Loading and unloading of a thick-walled cylinder of critical state soils: large strain analysis with applications

Dr. Pei-Zhi **Zhuang** [1,2,3], research fellow

Email: p.zhuang@leeds.ac.uk

Professor Hai-Sui **Yu** [2], FREng

Deputy Vice-Chancellor

E-mail: H.Yu@leeds.ac.uk

Professor Sacha Jon **Mooney** [4]

E-mail: sacha.mooney@nottingham.ac.uk

Dr. Pin-Qiang **Mo** [2], Associate Research Scientist

Corresponding author

pinqiang.mo@cumt.edu.cn

[1] School of Qilu Transportation, Shandong University, 250002, Jinan, China

[2] School of Civil Engineering, Faculty of Engineering,
University of Leeds, LS2 9JT Leeds, UK

[3] State Key Laboratory for Geomechanics and Deep Underground Engineering China University of Mining and Technology, 221116, Xuzhou, Jiangsu, China.

[4] School of Biosciences, University of Nottingham, LE12 5RD Leicestershire, UK

May 2020

Abstract

Thick-walled cylinder (TWC) tests are widely used to obtain soil properties and investigate wellbore instability problems in laboratory-controlled conditions. This paper presents analytical cavity expansion and contraction solutions for modelling undrained TWC tests under three typical loading and unloading programs. Both cylindrical and spherical cavities in critical state soils with a finite radial extent subjected to monotonic loading or unloading under undrained conditions are considered. The solutions are developed in terms of finite strain formulations, and the procedure is applicable to any isotropically hardening materials. Parametric studies show the boundary effect may significantly affect the cavity expansion/contraction response. A limit outer-to-inner diameter ratio of the soil sample exists, beyond which the boundary effect becomes negligible. The limit ratio varies with the cavity geometry, soil stress history (OCR), and cavity deformation level. For undrained TWC tests, a diameter ratio over 20 should normally be adequate to remove the possible boundary effect. Predicted expansion and contraction curves by the new solutions are compared with published data of TWC tests in the literature, and good agreement is shown in each loading/unloading program. This indicates that the boundary effect, which greatly limits the application of conventional cavity expansion/contraction solutions into TWC problems, is successfully captured by the present solutions. The solutions can also serve as valuable benchmark for verifying various numerical methods involving critical state plasticity models.

KEYWORDS: Cavity expansion, Cavity contraction, Thick-walled cylinder tests, Boundary effect, Critical state soil

1 Introduction

Loading and unloading of a thick-walled cylinder (TWC) of soil in a triaxial cell or chamber have been used to investigate the soil behaviour involved in a wide class of geotechnical problems [3,5,27,36]. In laboratory-controlled conditions, three loading/unloading programs are commonly applied in TWC tests, namely internal loading (i.e. increasing the internal pressure), internal unloading (i.e. reducing the internal pressure) and external loading (i.e. increasing the external pressure), while keeping other confining pressures constant [1] (see Fig. 1). The internal loading program (also known as the boundary condition BC1 [27]) is often used to investigate the pressuremeter response [6,26,31,33,35,58]; the internal unloading and external loading programs are common in the study of wellbore instability problems [1,18,24,74].

For the purpose of saving energy, time, cost and space during sample preparation and testing and/or improving detectability or traceability of internal soil deformation with non-destructive measurement techniques (e.g. X-ray Computed Tomography), hollow cylinder triaxial apparatuses with outer-to-inner diameter ratios (or chamber diameter to pressuremeter diameter ratio) in a range of 2 to 20 have widely been used in the laboratory [3,5,6,23,26,31,33-36,43,58,60]. It has been reported that significant boundary effects (or container size effect) usually exist in the loading and unloading tests within such small-sized containers, which may lead the measured soil response to be quite different from that in an infinite or 'semi-infinite' soil mass [3,25,29,35,47,49,54,55]. Cavity expansion/contraction theory is a useful theoretical tool for the study of pressuremeter tests and wellbore instability problems [14,18,28,32,42,71]. However, the focus of most previous studies has been on the analysis of a cavity embedded in an infinite soil mass ideally simulating the field conditions [69]. The aforementioned boundary effect is apparently overlooked in these infinite cavity expansion and contraction models. Consequently, they are not suitable for the analysis of pressuremeter and wellbore instability problems in TWC tests as discussed by Juran and BenSaid [34], Silvestri [57], and Abdulhadi [1], among others. To address this problem, this paper presents novel and general solution procedures for undrained cavity expansion and contraction analysis in soils with a finite radial extent under the aforementioned three loading/unloading programs, and a set of analytical/semi-analytical finite strain solutions for several Cam-Clay-type soil models is derived.

Before presenting the theoretical analysis, some pioneering studies into quasi-static cavity expansion and contraction behaviour under the considered loading/unloading programs are briefly reviewed. For a cavity expanding and contracting in an infinite soil mass under the internal loading and unloading programs, undrained expansion and contraction solutions in the framework of critical state soil mechanics refer to some pioneering works from Collins and Yu [22], Chen and Abousleiman [15], Vrakas [61], Mo and Yu [40] and Yu and Rowe [73], Vrakas and Anagnostou [62], Chen and Abousleiman [17], Mo and Yu [39], respectively. For brevity, we focus here on reviewing relevant elastic-plastic solutions for the analysis of a cavity embedded in a finite soil mass as below.

Existing analytical solutions for the problem of an internally pressurized cavity within a finite soil mass are mainly restricted to elastic-perfectly plastic models such as the Tresca model [30,34,69] and Mohr-Coulomb model [25,48,66,67]. When considering the hardening and softening behaviour of soil, a few semi-analytical drained solutions have also been developed so far. Salgado et al. [53] presented solutions for expansion analysis of a cylindrical cavity in Mohr-Coulomb soils considering non-linear elasticity and variations of friction and dilation angles. The solution was combined with stress rotation analysis to investigate the effects of several types of boundaries to the cone penetration resistance in sand [54]. Adopting an elastic-plastic constitutive model formulated in the critical state framework, Pournaghiazar et al. [48] developed approximate solutions using the similarity technique for both cylindrical and spherical cavities expanded from zero radius subjected to either constant stress or zero displacement at the finite boundary under drained conditions. For the same problem, a more rigorous spherical solution was obtained by Cheng and Yang [19] with the aid of the auxiliary independent variable proposed by Chen and Abousleiman [16]. Cheng et al. [20] further applied the method to the cavity expansion analysis in a finite unsaturated soil mass assuming that the contribution of suction to the effective stress is constant. Lately, Wang et al. [63] derived a solution for a spherical cavity expanding in modified Cam Clay of finite radial extent under undrained conditions. The development of these solutions highly relied on the assumption that the conditions at the elastic-plastic boundary satisfy the plastic and elastic governing equations simultaneously. This requires that the radius of the elastic-plastic boundary must always be smaller than the outer radius of the finite soil medium upon loading, which may valid for the cavity creation or cone penetration problems that were studied in these references. However, this is not generally appropriate for the loading analysis of a hollow cylinder or spherical shell with small outer-to-inter diameter ratios as the entire soil mass may easily yields plastically [49,66,67], in particular for normally consolidated soils. In more general conditions, existing studies into this problem were mainly based on numerical techniques [4,11,35,49].

The external loading and internal unloading programs have often been applied in both laboratory tests [1,24,45] and numerical simulations [4,44,74] of TWCs, but a very limited number of analytical solutions were obtained for these cavity contraction problems in a finite soil mass. Durban and Papanastasiou [24] presented semi-analytical solutions for the external compression analysis of a thick-walled cylinder using non-associated Mohr-Coulomb and Drucker-Prager models with arbitrary hardening. Very recently, focusing on the short-term contraction behaviour of soil around shallow tunnels in clay, Zhuang et al. [75] presented a set of undrained cavity contraction solutions for both thick-walled cylinders and spherical shells of Cam clays under the internal unloading program in the companion paper. However, solutions for undrained contraction analysis under the external loading program are not common in the literature to the best knowledge of the authors, particularly for advanced critical state models of soil.

In the light of the above discussion, the novelty and importance of the present solutions mainly lie in the following: (a) three typical loading/unloading programs that commonly used in TWC tests are considered, and the associated boundary effect is captured in a rigorous semi-analytical manner; (b) the strain is finite, and the solution procedure applicable for any isotropically hardening materials; and (c) the solution for the unified state parameter model of CASM [68] is able to describe the cavity expansion and contraction behaviour in both clay (including heavily overconsolidated clay) and sand. The paper is structured as follows: Section 2 defines the problem; Section 3 presents the general solution procedure first, which is followed by solutions for several critical state soil models; Section 4 gives results of model validation and parametric studies; Section 5 shows comparisons between predicted and measured cavity expansion and contraction curves for TWC tests under three different loading and unloading programs. Finally, some conclusions are drawn.

2 Problem Definition

As depicted in Fig.1, in a hollow cylinder triaxial cell, the soil specimen is subjected to three independently controlled confining stresses: the axial stress (p_a), the uniform radial pressures acting on the inner (p_{in}) and outer (p_{out}) surfaces. The height, the inner and outer diameters of the hollow cylinder specimen are denoted by H_t, D_i and D_o, respectively. It has been shown that, with constant axial confining stress, the height of the specimen has minimal effect on the radial expansion or contraction response as long as the ratio of H_t/D_o is greater than 1.5 [1,3]. In this case, the hollow cylinder loading/unloading tests can be ideally modelled as plane-strain cylindrical cavity expansion/contraction problems. In Fig.1, the inner and outer radii of a soil annulus upon radial loading or unloading are expressed by a and b , respectively, and a_0 and b_0 represent their initial values, respectively.

It was previously introduced that three typical loading/unloading modes (named as internal loading, internal unloading and external loading) are often applied in TWC tests for investigating pressuremeter and borehole instability problems in the laboratory. In the internal loading or unloading program, the internal radial pressure is increased or decreased monotonically, while keeping the external cell pressure and the axial confining stress constant [3,35,58]. With the external loading program, TWC tests are performed by increasing the external cell pressure, while keeping the internal cavity pressure and the axial stress constant [1,24,74]. In general, the rate of loading/unloading in TWC tests under undrained conditions is much faster than the rates of consolidation and creep of soil [2,4,58], hence the behaviour of soil is considered as rate-independent in this study.

The TWC tests subjected to monotonic loading or unloading are transformed into a typical boundary value problem of one-dimensional quasi-static cavity expansion or contraction. It has been shown that the analyses of spherical and long cylindrical cavity problems under uniform stress conditions are quite similar and can be treated simultaneously by introducing a parameter k (k is equal to 1 for a cylindrical cavity and 2 for a spherical cavity) [12,22,72,73]. Hence, solutions for the analysis of a thick-wall spherical shell of soil are also derived. The spherical expansion and contraction solutions may offer a chance to model point injection tests (e.g. Au et al. [8]) and cone penetration tests(e.g. Cheng and Yang [19] in small sized calibration chambers and spherical sinkhole formation problems at shallow depths (e.g. Augarde et al. [9]), but this is considered beyond the scope of this paper.

For convenience, cylindrical coordinates (r, θ, z) and spherical coordinates (r, θ, φ) with the origin located at the centre of the cavity are employed for the analysis of thick-walled cylinder and spherical shell, respectively. The cylindrical cavity expansion/contraction analyses are performed under plane strain conditions with respect to the z-axis. Taking compression as positive, the initial stress boundary conditions are expressed as:

$$\sigma_r\big|_{r=a_0} = p_0 \quad , \quad \sigma_r\big|_{r=b_0} = p_0 \tag{1 a,b}$$

where σ_r represents the total radial stress. r is the current radial coordinate of a material element which was initially at r_0. p_0 is the initial total confining pressure. $p_0 = p_0' + U_0$, p_0' is the initial mean effective stress, and U_0 is the initial ambient pore pressure.

The expansion and contraction analyses are performed under undrained conditions. The surrounding soil is assumed to be homogeneous and isotropic. For convenience, the mean effective and deviatoric stresses (p', q) below are used for the quasi-static analysis of the axisymmetric cavity expansion/contraction problem following Collins and Yu [22] and Yu and Rowe [73].

$$p' = \frac{\sigma_r' + k\sigma_\theta'}{1+k} \quad , \quad q = \sigma_r' - \sigma_\theta' \tag{2 a,b}$$

where σ_r' and σ_θ' are the effective radial and circumferential stresses, respectively.

The volumetric and shear strains (δ ; γ) are defined as:

$$\delta = \varepsilon_r + k\varepsilon_\theta \quad , \quad \gamma = \varepsilon_r - \varepsilon_\theta \tag{3 a,b}$$

where ε_r and ε_θ are radial and circumferential strains, respectively. It needs to be pointed out that for the cylindrical case the above definitions for the stress and strain invariants are slightly different from the usual three-dimensional definitions in critical state soil models. However, it has been shown (e.g. in references of Sheng et al. [56] and Chen and Abousleiman [15]) that the error due to these simplifications is negligible for the analysis of cylindrical cavity problems under an isotropic in-situ stress state which is of interest in this paper.

3 Undrained cavity expansion/contraction analysis

3.1 Governing equations

Quasi-static cavity expansion/contraction analysis is mainly concerned with two typical problems: (a) continuous pressure-displacement curves; and (b) stress and strain distributions in soil at a given instant. Solutions for them can be obtained by solving a set of equations of stress equilibrium, deformation compatibility and stress-strain relationships of soil (as defined below) with given boundary conditions.

(1) Stress equilibrium

Under uniform and monotonic loading or unloading, neglecting body force and dynamic effect, the stress equilibrium condition along the radial direction can be expressed in terms of total stresses (Eulerian description) as:

$$\sigma_r - \sigma_\theta + \frac{r}{k}\frac{\mathrm{d}\sigma_r}{\mathrm{d}r} = 0 \tag{4}$$

where σ_θ is the total circumferential stress.

Since $\sigma_r = p + kq/(k+1)$ and $U = p - p'$ (p : the mean total pressure; U : the pore pressure), the gradient of U along the radial direction is given as:

$$\frac{\mathrm{d}U}{\mathrm{d}r} = -\frac{\mathrm{d}p'}{\mathrm{d}r} - \frac{k}{k+1}\frac{\mathrm{d}q}{\mathrm{d}r} - \frac{k}{r}q \tag{5}$$

(2) Deformation compatibility

For the axisymmetric cavity expansion/contraction problem under undrained conditions, the constant-volume condition can be expressed as:

$$a^{k+1} - a_0^{k+1} = r^{k+1} - r_0^{k+1} = T \tag{6}$$

where T is the variable representing the volumetric change of soil at an arbitrary radius.

While keeping the external confining pressure constant, internal loading will lead to outward expansions of the surrounding soil, whereas inward contractions will be caused by internal unloading. Compressive deformation is taken as positive in this paper. Based on Eq. (6), the corresponding deformation compatibility equations for these two cases can be readily obtained [22,73]. Rigorous relations between the finite shear strain and the radial coordinate without any restriction on the deformation level are given: (a) for a given particle (i.e. Lagrangian description in Eq. (7)), and (b) at a fixed instant of time (i.e. Eulerian description in Eq. (8)), respectively, as:

$$\gamma = \ln\left[\frac{r_0^{k+1} + T}{r_0^{k+1}}\right] = (k+1)\ln\frac{r}{r_0} \qquad \text{(internal loading/unloading)} \qquad (7)$$

$$\gamma = -\ln\left[1 - \frac{T}{r^{k+1}}\right] \qquad \text{(internal loading/unloading)} \qquad (8)$$

Hence relations between the radial coordinate and shear strain increments: (a) for a given particle, and (b) at a fixed instant of time, respectively, are:

$$(k+1)\frac{\mathrm{d}r}{r} = \mathrm{d}\gamma \quad , \quad (k+1)\frac{\mathrm{d}r}{r} = -\frac{\mathrm{d}\gamma}{\exp(\gamma)-1} \qquad \text{(internal loading/unloading)} \qquad (9\text{ a, b})$$

In the external loading program, the surrounding soil moves inwards (i.e. cavity contraction) with increasing external pressures. The soil movement is similar to that which occurred in the internal unloading program, but the soil deforms under compression. Therefore, new relations between the finite shear strain and the radial co-ordinate are constructed in Eqs. (10) and (11), which are: (a) for a given particle, and (b) at a fixed instant of time, respectively.

$$\gamma = -\ln\left[\frac{r_0^{k+1} + T}{r_0^{k+1}}\right] = -(k+1)\ln\frac{r}{r_0} \qquad \text{(external loading)} \qquad (10)$$

$$\gamma = \ln\left[1 - \frac{T}{r^{k+1}}\right] \qquad \text{(external loading)} \qquad (11)$$

and the incremental expressions of these relations become:

$$(k+1)\frac{\mathrm{d}r}{r} = -\mathrm{d}\gamma \quad , \quad (k+1)\frac{\mathrm{d}r}{r} = -\frac{\mathrm{d}\gamma}{\exp(-\gamma)-1} \qquad \text{(external loading)} \qquad (12\text{ a,b})$$

(3) Stress-strain relationships

The stress-strain relationships are conveniently defined in general forms appropriate for a wide class of two-invariant critical state soil models in this subsection. Before entering plastic, soil behaviour is purely elastic. The elastic constitutive law is expressed in rate forms as:

$$\dot{\delta}^e = \frac{\overset{\circ}{p'}}{K(p',v)} \quad , \quad \dot{\gamma}^e = \frac{\overset{\circ}{q}}{2G(p',v)} \qquad (13\text{ a,b})$$

where $\dot{\delta}^e$ and $\dot{\gamma}^e$ represent the elastic volumetric and shear strain rates, respectively. $K(p',v)$ and $G(p',v)$ are the instantaneous bulk and shear moduli, which are pressure-dependent (e.g. Eq.14). v is the specific volume. The symbol $(\overset{\circ}{\ })$ denotes the material time derivative associated with a given material particle; $(\overset{\bullet}{\ })$ denotes the local time derivate, evaluated at a fixed position r.

The hypoelastic model that commonly adopted in Cam-Clay-type models (e.g. Table 1) can be recovered by combining Eqs. (13) and (14).

$$K(p',v) = vp'/\kappa \quad , \quad G(p',v) = \varpi \frac{vp'}{\kappa} \tag{14 a,b}$$

where $\varpi = 0.5[(1+k)(1-2\mu)]/[1+(k-1)\mu]$, and μ denotes Poisson's ratio of soil. κ denotes the slope of the swelling line in the v - $\ln p'$ space.

The loading and unloading programs are treated in a single analysis by introducing a parameter ς (i.e. $\varsigma = 1$ for internal and external loading; $\varsigma = -1$ for internal unloading) in this paper. Then the yield function and the plastic flow rule that used to describe the plastic behaviour of soil (e.g. Table 1) are written in a general form as:

$$q = f(p', p'_y) \quad , \quad \frac{\dot{\delta}^p}{\dot{\gamma}^p} = \frac{\partial g / \partial p'}{\partial g / \partial q} = D(\eta) \tag{15a,b}$$

where g is the plastic potential; $D(\eta)$ represents the stress–dilatancy function; $\eta = \varsigma q / p'$, is the stress ratio. p'_y denotes the preconsolidation pressure, which controls the size of the yield surface as a hardening parameter. In usual Cam-Clay type soil models [50,51,68], hardening is attributed solely to accumulated plastic volumetric strains, and the volumetric hardening rule of Eq.(16) is usually adopted.

$$\mathrm{d}\delta^p = \frac{(\lambda - \kappa)}{v} \frac{\mathrm{d}p'_y}{p'_y} \tag{16}$$

where λ denotes the slope of the normal consolidation line (NCL) in the v - $\ln p'$ space.

Table 1 Critical state constitutive models considered in the present study.

Model	Yield function	Stress–dilatancy function $D(\eta)^*$
Original Cam-Clay [51]	$q = \varsigma M p' \ln(p'_y / p')$	$D(\eta) = \varsigma \frac{k}{(k+1)}(M - \eta)$
Modified Cam-Clay [50]	$q = \varsigma M p' \sqrt{p'_y / p' - 1}$	$D(\eta) = \varsigma \frac{k}{(k+1)} \frac{M^2 - \eta^2}{2\eta}$
CASM [68]	$q = \varsigma M p' \left[-\frac{\ln(p'/p'_y)}{\ln r^*} \right]^{1/n}$ §	$D(\eta) = \varsigma \frac{k}{(k+1)} \frac{9(M-\eta)}{(9+3M-2M\eta)}$

* Note that the conjugate shear strain to the shear stress of Eq. (2b) is in the form of $\varepsilon_q = k\gamma/(k+1)$. Accordingly, expressions of $D(\eta)$ are modified by definition.

§ n and r^* are the stress-state coefficient and the spacing ratio, respectively. r^* controls the intersection position of the the critical state line (CSL) and the yield surface; n defines the shape of the yield surface (see Fig.2) in CASM [68].

The critical state is defined by the following two equations [52].

$$v = \Gamma - \lambda \ln p' \tag{17}$$

$$q = \varsigma M p' \tag{18}$$

where Γ is the value of v on the CSL at p'=1kPa . M is the slope of the CSL in the p'-q space, which can be expressed as $M = \left[2(k+1)\sin\varphi_{cs}\right]/\left[(k+1)-(k-1)\sin\varphi_{cs}\right]$ for the present problem with Eq. (2). φ_{cs} is the critical state friction angle of soil. It has been shown that φ_{cs} measured in plane strain tests is up to 10-20% larger than that in triaxial compression tests (φ_{tc}) due to the shear mode effect (or intermediate effective stress effect) [13,65]. To account for this effect in the analysis, it is assumed that φ_{cs} equals 1.1-1.2 times of φ_{tc} for the plane strain conditions (k=1) and $\varphi_{cs} = \varphi_{\mathrm{tc}}$ for the spherical symmetric conditions (k=2) [20].

3.2 Analytical effective stress analysis under undrained loading and unloading

The above stress-strain relationships define that one soil element may successively enter three stress states (including purely elastic state, elastic-plastic state, and critical state) upon monotonic loading or unloading. Solutions for each state are derived as follows.

(1) Purely elastic state

According to the constant-volume condition and Eq. (13a), the mean effective stress remains constant and equals its initial value p'_0 at the purely elastic state. Therefore, the bulk and shear moduli also remain constant and equal to their initial values K_0 and G_0 respectively. The elastic shear stress q^e can be obtained by integrating Eq. (13b) along a particle path as:

$$q^e = 2G_0\gamma \tag{19}$$

Then the effective radial and circumferential stresses ($\sigma_r'^e$ and $\sigma_\theta'^e$) are given as:

$$\sigma_r'^e = p_0' + \frac{k}{k+1} q^e \quad , \quad \sigma_\theta'^e = p_0' - \frac{1}{k+1} q^e \tag{20}$$

(2) Elastic-plastic state

The soil yields plastically when the shear stress invariant reaches the yield value of q_{ep}, which will depend upon the particular yield criterion. According to Eqs. (7) (or (10)) and (19), plastic deformation occurs first at the inner wall of the cavity upon loading or unloading, and the corresponding limit elastic shear strain equals:

$$\gamma_{ep} = \frac{q_{ep}}{2G_0} \tag{21}$$

The plastic zone propagates outwards with subsequent loading or unloading. From Eqs. (8) (or (11)) and (21), the current and initial radii of the elastic-plastic boundary (c and c_0, respectively) at the instant of the cavity with a radius of a under different loading/unloading programs can be expressed, respectively, as:

$$\left(\frac{c}{a}\right)^{k+1} = \frac{(a_0/a)^{k+1}-1}{\exp(-\gamma_{ep})-1} \quad , \quad c_0 = (c^{k+1}+T)^{\frac{1}{k+1}} \quad \text{(internal loading/unloading)} \tag{22a,b}$$

$$\left(\frac{c}{a}\right)^{k+1} = \frac{(a_0/a)^{k+1}-1}{\exp(\gamma_{ep})-1} \quad , \quad c_0 = (c^{k+1}+T)^{\frac{1}{k+1}} \quad \text{(external loading)} \tag{23a,b}$$

As $\dot{\delta}^e + \dot{\delta}^p = 0$ under undrained conditions, integrating Eqs. (13a) and (16) gives:

$$\kappa \ln\left(\frac{p'}{p_0'}\right) + (\lambda-\kappa)\ln\left(\frac{p_y'}{p_{y0}'}\right) = 0 \tag{24}$$

Eq. (24) defines a relationship between the hardening parameter p_y' and the mean effective stress, by which the functions of $f(p', p_y')$ and $D(\eta)$ in Eqs. (15 a,b) can be explicitly converted into functions in terms of p' solely (e.g. Table 2). Then the total elastic-plastic shear strain rate $\dot{\gamma}$ can be expressed into Eq. (25) based on the constant-volume condition and Eqs. (13)-(16).

$$\dot{\gamma} = \dot{\gamma}^e + \dot{\gamma}^p = L(p')\overset{\circ}{p'} \tag{25}$$

where

$$L(p')=\frac{q'(p')}{2G(p')}-\frac{1}{K(p')D(\eta)} \quad (26)$$

Integrating Eq.(25) in terms of p' along a particle path starting from the initial yield time, at which $p' = p_0'$ and $q = q_{ep}$, gives an expression of γ as:

$$\gamma = \gamma_{ep} + I(p') - I(p_0') \quad (27)$$

where

$$I(p')=\int^{p'} L(p')\mathrm{d}p' \quad (28)$$

Note that Eqs. (24)-(28) suit for any case of stress-controlled proportional loading or unloading under undrained conditions [46], which certainly includes the loading/unloading programs considered in this study.

(3) Critical state

Under undrained conditions, the specific volume of soil remain unchanged. Therefore, once the soil has reached the critical state, the mean effective stress and shear stress remain constant (i.e. p_{cs}' and q_{cs}, respectively) as defined by in Eqs. (17) and (18), values of which will depend upon the particular yield criterion.

(4) Solution procedure for effective stresses

Taking the CASM model [68] as an example, here the procedure to derive the functions of $I(p')$ and $L(p')$ is further detailed. Based on Eq. (24), the yield function of CASM (see Table 1) is converted into Eq. (29) in terms of p', which is required for obtaining an explicit expression of $L(p')$.

$$q(p') = \varsigma Mp\left[A_1 + A_2 \ln p'\right]^{1/n} \quad (29)$$

in which

$$A_1 = \frac{\ln R_0 + \Lambda^{-1}\ln p_0'}{\ln r^*}, \quad A_2 = -\frac{\Lambda^{-1}}{\ln r^*}, \text{ and } \Lambda = \frac{\lambda - \kappa}{\lambda}. \quad (30\text{ a,b,c})$$

where R_0 is the isotropic over-consolidation ratio, defines as p_{y0}' / p_0'. p_{y0}' is the initial value of p_y'. R_0 is different from the usual one-dimensional definition of the over-consolidation ratio (i.e. OCR), and relationships between R_0 and OCR refer to the references of Wood [64], Yu and Collins [71] and Chang et al. [13]. Eq. (29) can recover the yield surface of the original Cam-Clay model exactly by choosing $n=1$ and $r^*=2.718$ (e.g. Fig.2a); the 'wet' side of the modified Cam-Clay model can be approximated by choosing $r^*=2$ in conjunction with a suitable value of n (e.g. Fig.2b).

With the given constitutive equations of CASM and Eq. (26), the function of $L(p')$ is obtained as:

$$L(p')=\varsigma\frac{\kappa}{vp'}\left\{\frac{M}{2\varpi}\left[\left(A_1+A_2\ln p'\right)^{1/n}+\frac{A_2}{n}\left(A_1+A_2\ln p'\right)^{1/n-1}\right]-\frac{\left(k+1\right)}{k}\frac{\left(9+3M-2M\eta\right)}{9(M-\eta)}\right\} \quad (31)$$

Then integrating Eq. (31) in terms of p' along the stress history of a particle gives:

$$\begin{aligned}I(p')=&\varsigma\frac{\kappa M}{2\varpi v}\left[\frac{n}{(1+n)A_2}\left(A_1+A_2\ln p'\right)^{\frac{1}{n}+1}+\left(A_1+A_2\ln p'\right)^{\frac{1}{n}}\right]\\&-\varsigma\frac{\kappa n(m+1)}{9vA_2M^n m}\left[\frac{2M}{n}\eta^n+\left(9+3M-2M^2\right)\int\frac{\eta^{n-1}}{M-\eta}\mathrm{d}\eta\right]\end{aligned} \quad (32)$$

in which

$$\int\frac{\eta^{n-1}}{M-\eta}\mathrm{d}\eta=\frac{\eta^n\left[n\eta\,{}_2F_1\left(1,n+1;n+2;\eta/M\right)+M(n+1)\right]}{n(n+1)M^2} \quad (33)$$

where ${}_2F_1\left(1,n+1;n+2;\eta/M\right)$ is the Gaussian hypergeometric function in terms of η/M.

With $p'=p'_0$, Eq. (29) gives the elastic limit of the shear stress in Eq. (34).

$$q_{ep}=\varsigma\left(\frac{\ln R_0}{\ln r^*}\right)^{\frac{1}{n}}Mp'_0 \quad (34)$$

Then by substituting Eq. (34) into Eq. (21), the elastic limit of the shear strain (γ_{ep}) required for the determination of the finite shear strain in Eq.(27) is known.

Similarly, solutions of $I(p')$ and $L(p')$ for the widely used original and modified Cam-Clay models are also derived as given in Table 2. The above procedure is applicable for any constitutive model in the form of that defined in the last subsection.

Table 2 Solutions of $I(p')$ and $L(p')$ for original and modified Cam-Clay models.

Model	Solutions

Original Cam-Clay	$q(p') = -\varsigma M p' \left(\frac{1}{\Lambda} \ln \frac{p'}{p'_0} - \ln R_0 \right)$, $q_{ep} = \varsigma M p'_0 \ln R_0$ $L(p') = -\varsigma \left\{ M \left(\frac{1}{\Lambda} + \frac{1}{\Lambda} \ln \frac{p'}{p'_0} - \ln R_0 \right) \frac{\kappa}{2\varpi v p'} + \frac{(k+1)}{k} \frac{\kappa}{v p'(M-\eta)} \right\}$ $I(p') = -\varsigma \left\{ \frac{\kappa M}{2\varpi v} \left[\frac{1}{2\Lambda} (\ln p')^2 + \left(\frac{1}{\Lambda} - \frac{1}{\Lambda} \ln p'_0 - \ln R_0 \right) \ln p' \right] + \frac{(k+1)}{k} \frac{\kappa \Lambda}{v M} \ln (M-\eta) \right\}$
Modified Cam-Clay	$q(p') = \varsigma M p' \sqrt{R_0 (p'/p'_0)^{-1/\Lambda} - 1}$, $q_{ep} = \varsigma M p'_0 \sqrt{R_0 - 1}$ $L(p') = \varsigma \left\{ \frac{\kappa M}{2\varpi v p'} \frac{\left(1 - \frac{1}{2\Lambda}\right)\left((\frac{\eta}{M})^2 + 1 \right) - 1}{\eta / M} - \frac{(k+1)}{k} \frac{\kappa}{v p'} \frac{2\eta}{(M^2 - \eta^2)} \right\}$ $I(p') = \varsigma \left\{ \frac{\kappa}{2\varpi v} \left[(1-2\Lambda)\eta + 2M\Lambda \tan^{-1} \frac{\eta}{M} \right] + \frac{2(k+1)}{k} \frac{\kappa \Lambda}{v M} \left[\tanh^{-1} \frac{\eta}{M} - \tan^{-1} \frac{\eta}{M} \right] \right\}$

Once the soil has reached the critical state, the mean effective stress and shear stress remain constant (i.e. p'_{cs} and q_{cs}, respectively) under undrained conditions. For the constitutive models listed in Table 1, p'_{cs} and q_{cs} can be expressed as:

$$p'_{cs} = p'_0 \left(\frac{R_0}{r^*} \right)^{\Lambda} = \exp\left(\frac{\Gamma - v}{\lambda} \right) \quad , \quad q_{cs} = \varsigma M p'_{cs} \qquad (35\text{ a,b})$$

where r^*=2.718 and r^*=2 for the original and modified Cam clays, respectively.

In the above, the shear strain was expressed in two ways by means of strain compatibility analyses and integrations of the stress-strain relationships, respectively. Based on them, the effective stresses in the soil can be readily related to the kinematic process of cavity expansion/contraction. In summary, (a) during purely elastic loading or unloading, p' remains constant as p'_0, and q can be obtained by Eq.(19) in conjunction with the compatibility relations (i.e. Eqs. (7), (8), (10) and (11)); (b) in the elastic-plastic state, continuous changes of the effective stresses in a given soil element upon loading or unloading can be determined by equalling Eq. (27) with Eq. (7) (or Eq. (10)), and distributions of the effective stresses along the radial coordinate at a fixed instant can be determined by equalling Eq. (27) with Eq. (8) (or Eq. (11)); (c) in the critical state, both p' and q remain constants as defined in Eq. (35).

3.3 Calculation of excess pore pressures

The excess pore pressure (ΔU) at a given instant can be determined by integrating Eq. (5) along the radial direction. Although all soil particles go through the same effective stress path, the total stress path of each element varies along the radial direction due to the difference in the total pressure between the inner and outer boundaries of the finite soil mass [35]. This is different to the self-similar cavity expansion or contraction problem in an infinite soil mass and makes the solution procedure for obtaining ΔU become more complicated. A general solution procedure for this typical non-self-similar boundary value problem is developed as follows.

(1) Solutions for a cavity under loading or unloading

In the internal loading or unloading program, the total radial pressure at the outer boundary (i.e. $r=b$) is kept constant. With Eq. (9b), integrating Eq. (5) from $r=b$ gives:

$$\Delta U\big|_r = \Delta U\big|_b - (p'\big|_r - p'_b) - \frac{k}{k+1}(q\big|_r - q_b) + \frac{k}{k+1}\int_{\gamma_b}^{\gamma} \frac{q\mathrm{d}\gamma}{\exp(\gamma)-1} \tag{36}$$

where $\Delta U\big|_r$, $p'\big|_r$ and $q\big|_r$ are excess pore pressure, mean effective stress and shear stress at an arbitrary radius of r. γ_b and $\Delta U\big|_b$ are the shear strain and the excess pore pressure at $r=b$, respectively.

It is clear that $\Delta U\big|_r$ depends on the effective stress states of soil at both $r=b$ and the position of concern. According to the stress state at both positions, it is found that six phases possibly occur. To facilitate the calculation of $\Delta U\big|_r$, Eq. (36) can be simplified into different forms at different phases as follows.

(a) Purely elastic phase (elastic at both $r=b$ and $r=a$)

While the entire soil mass stays at the purely elastic state, the mean effective stresses in the whole field remain constant and equal p'_0. The shear stresses are known with Eq. (19). Hence, by simplifying Eq. (36), a closed-form solution for $\Delta U\big|_r$ in the elastic region is obtained as:

$$\Delta U\big|_r = -\frac{k}{k+1}q + \frac{2G_0 k}{k+1}\int_{\gamma_b}^{\gamma} \frac{\gamma\mathrm{d}\gamma}{\exp(\gamma)-1} \tag{37}$$

in which

$$\int \frac{\gamma \mathrm{d}\gamma}{\exp(\gamma)-1} \doteq -\sum_{i=1}^{\infty} \frac{\left[1-\exp(\gamma)\right]^i}{i^2} - \frac{\gamma^2}{2} \tag{38}$$

(b) Elastic-plastic phase (elastic at $r = b$ and plastic at $r = a$)

Upon further loading or unloading, soil particles enter the plastic state first at the inner cavity wall. Subsequently, the plastic region propagates outwards, the radius of which can be determined by Eq. (22). In the elastic-plastic phase that the soil at $r = b$ remains elastic while the soil at $r = a$ yields plastically already, $\Delta U|_r$ in the outside elastic region can be calculated by Eq. (37). Thus the excess pore pressure at the elastic-plastic boundary (i.e. $\Delta U|_{r=c}$) is obtained as the shear strain therein (i.e. γ_{ep}) is known from Eq. (21). Then the excess pore pressure within the inside plastic region is obtained from Eqs. (15a), (27) and (36) as:

$$\Delta U|_r = \Delta U|_{r=c} - (p' - p'_0) - \frac{k}{k+1}\left[q - q_{ep} - J_{partial}\right] \tag{39}$$

in which

$$J_{partial} = \int_{\gamma_{ep}}^{\gamma} \frac{q \mathrm{d}\gamma}{\exp(\gamma)-1} = \int_{p'_0}^{p'} \frac{q L(p') \mathrm{d}p'}{\exp(\gamma)-1} \tag{40}$$

With further loading or unloading, two phases may appear according to the stress states at $r = b$ and at $r = a$. One is that the soil at $r = a$ enters the critical state while the soil at $r = b$ still stays as elastic. The other is that the soil at $r = b$ yield plastically before the soil at $r = a$ enters the critical state. The sequence of occurrence of these two phases mainly depends on the ratio of b_0 / a_0 and the stress history (e.g. R_0). Therefore, solutions for them are given as follows in no particular order.

(c) Elastic-critical-state phase (elastic at $r = b$ and critical state at $r = a$)

In this phase, elastic, plastic and critical state regions exist simultaneously within the surrounding soil from the outside in. $\Delta U|_r$ in the outside two regions can be calculated with the procedure for the analysis of the elastic-plastic phase. Hence, the value at the plastic-critical-state boundary $r = r_{cs}$ (i.e. $\Delta U|_{r=r_{cs}}$) can be obtained from Eq. (39) with inputs of the critical state effective stresses (i.e. p'_{cs} and q_{cs} in Eq. (35 a,b). Then $\Delta U|_r$ within the critical state region (i.e. $a \le r \le r_{cs}$) can be obtained from Eq. (36) as:

$$\Delta U\big|_r = \Delta U\big|_{r=r_{cs}} + \frac{kq_{cs}}{k+1}\ln\left[\frac{\exp(-\gamma)-1}{\exp(-\gamma_{cs})-1}\right] \tag{41}$$

where γ_{cs} is the shear strain at $r = r_{cs}$.

(d) Fully plastic phase (plastic at both $r = b$ and $r = a$)

In this case, Eq. (36) goes to:

$$\Delta U\big|_r = \Delta U\big|_{r=b} - (p' - p'_b) - \frac{k}{k+1}\left[q - q_b - J_{full}\right] \tag{42}$$

in which

$$J_{full} = \int_{\gamma_b}^{\gamma} \frac{q\mathrm{d}\gamma}{\exp(\gamma)-1} = \int_{p'_b}^{p'} \frac{qL(p')\mathrm{d}p'}{\exp(\gamma)-1} \tag{43}$$

At a known expansion/contraction instant, γ_b can be determined by Eqs. (6) and (7) as:

$$\gamma_b = (k+1)\ln\left[\left(b_0^{\,k+1} + T\right)^{1/(k+1)} \big/ b_0\right] \tag{44}$$

The mean effective stress at $r = b$ (i.e. p'_b) in this phase can thus be back-calculated by equalling Eqs. (27) and (44), and the shear stress at $r = b$ (i.e. q_b) is then known from the yield function. Finally, as the external radial total pressure is kept constant, $\Delta U\big|_{r=b}$ is obtained as:

$$\Delta U\big|_{r=b} = p'_0 - \left[p'_b + kq_b/(k+1)\right] \tag{45}$$

(e) Plastic-critical-state phase (plastic at $r = b$ and critical state at $r = a$)

Following the above phases, the soil at $r = a$ may enter the critical state upon further loading or unloading, which results in two stress regions within the surrounding soil, namely plastic and critical state regions from the outside in. Similarly, $\Delta U\big|_r$ within the outside plastic region can be determined taking the previous procedure for the fully-plastic phase (i.e. Eq. (42)); ΔU within the critical state region in this phase can be computed with Eqs. (41) and (42).

(f) Fully critical-state phase of expansions

If the entire soil mass enters the critical state, the excess pore pressures can be readily obtained from Eq.(36) as:

$$\Delta U = \Delta U\big|_{r=b}^{cs} + \frac{kq_{cs}}{k+1}\ln\left[\frac{\exp(-\gamma)-1}{\exp(-\gamma_b)-1}\right] \tag{46}$$

where $\Delta U\big|_{r=b}^{cs} = p_0' - \left[p_{cs}' + kq_{cs}/(k+1)\right]$.

(2) Solutions for a cavity under external loading

In the external loading program, the internal cavity pressure is kept constant. In this case, to determine the excess pore pressure $\Delta U\big|_r$ within the surrounding soil, Eq. (5) should be integrated from the inner cavity wall (i.e. $r=a$). With the use of Eq. (12b), the integration of Eq. (5) gives:

$$\Delta U\big|_r = \Delta U\big|_a - (p'\big|_r - p_a') - \frac{k}{k+1}(q\big|_r - q_a) + \frac{k}{k+1}\int_{\gamma_a}^{\gamma}\frac{q\,\mathrm{d}\gamma}{\exp(-\gamma)-1} \tag{47}$$

where $\Delta U\big|_a$, p_a' and q_a are the excess pore pressure, the mean effective stress and the plastic shear stress at $r=a$, respectively. γ_a is the shear strain at $r=a$.

According to Eqs. (6) and (47), $\Delta U\big|_r$ under the external loading program can be obtained in a similar procedure as that developed for the other two programs, although the paths of integration are opposite. The solution procedure is presented briefly as follow.

(a) Purely elastic phase (elastic at both $r=b$ and $r=a$)

By simplifying Eq. (47), $\Delta U\big|_r$ in the elastic region can be rewritten as:

$$\Delta U\big|_r = -\frac{k}{k+1}q + \frac{2G_0k}{k+1}\int_{\gamma_a}^{\gamma}\frac{\gamma\,\mathrm{d}\gamma}{\exp(-\gamma)-1} \tag{48}$$

in which

$$\int\frac{\gamma\,\mathrm{d}\gamma}{\exp(\gamma)-1} \doteq \sum_{i=1}^{\infty}\frac{\left[1-\exp(\gamma)\right]^i}{i^2} \tag{49}$$

At a given instant, γ_a can be calculated from Eqs. (6) and (10) as:

$$\gamma_a = -(k+1)\ln\left[\left(a_0^{k+1}+T\right)^{1/(k+1)}\Big/a_0\right] \tag{50}$$

(b) Elastic-plastic phase (elastic at $r=b$ and plastic at $r=a$)

The current and initial radii of the elastic-plastic boundary were given in Eqs. (23a,b). $\Delta U|_r$ within the inside plastic region (i.e. $a \le r \le c$) can be expressed as:

$$\Delta U|_r = \Delta U|_{r=a} - (p' - p'_a) - \frac{k}{k+1}\left[q - q_a - J_{partial}\right] \tag{51}$$

in which

$$J_{partial} = \int_{\gamma_a}^{\gamma} \frac{q\mathrm{d}\gamma}{\exp(-\gamma)-1} = \int_{p'_a}^{p'} \frac{qL(p')\mathrm{d}p'}{\exp(-\gamma)-1} \tag{52}$$

The mean effective stress p'_a can be back-calculated by equalling Eqs. (27) and (50), and the plastic shear stress q_a is then known from the yield function. As the internal radial pressure is kept constant, $\Delta U|_{r=a}$ equals:

$$\Delta U|_{r=a} = p'_0 - \left[p'_a + kq_a/(k+1)\right] \tag{53}$$

The excess pore pressure at the elastic-plastic boundary ($\Delta U|_{r=c}$) can then be computed by inputting $p' = p'_0$ and $q = q_{ep}$ into Eq. (51). Substituting the above values into Eq. (47), $\Delta U|_r$ within the outside elastic region is obtained as:

$$\Delta U|_r = \Delta U|_{r=c} - \frac{k}{k+1}(2G_0\gamma - q_{ep}) + \frac{2kG_0}{k+1}\int_{\gamma_c}^{\gamma} \frac{\gamma\mathrm{d}\gamma}{\exp(-\gamma)-1} \tag{54}$$

(c) Elastic-critical-state phase (elastic at $r = b$ and critical state at $r = a$)

At this phase, $\Delta U|_r$ in the inside critical state region (i.e. $a \le r \le r_{cs}$) can be obtained as:

$$\Delta U|_r = \Delta U|_{r=a} + \frac{kq_{cs}}{k+1}\ln\left[\frac{\exp(\gamma_a)-1}{\exp(\gamma)-1}\right] \tag{55}$$

With Eq. (55), the excess pore pressure at $r = r_{cs}$ (i.e. $\Delta U|_{r=r_{cs}}$) can be determined with inputs of p'_{cs} and q_{cs}. Taking the stress conditions at $r = r_{cs}$ as the initial values, $\Delta U|_r$ in the outside two regions can be calculated taking the above procedure for the analysis of the elastic-plastic phase.

(d) Fully plastic phase (plastic at both $r = b$ and $r = a$)

In this phase, Eq. (47) can be simplified to be:

$$\Delta U\big|_r = \Delta U\big|_{r=a} - (p' - p'_a) - \frac{k}{k+1}\left[q - q_a - J_{full}\right] \tag{56}$$

in which

$$J_{full} = \int_{\gamma_a}^{\gamma} \frac{q\mathrm{d}\gamma}{\exp(-\gamma)-1} = \int_{p'_a}^{p'} \frac{qL(p')\mathrm{d}p'}{\exp(-\gamma)-1} \tag{57}$$

Stresses at $r = a$ can be obtained with the same method that was just introduced above.

(e) Plastic-critical-state phase (plastic at $r = b$ and critical state at $r = a$)

At this phase, $\Delta U\big|_r$ within the inside critical state region can be computed using Eq. (55); $\Delta U\big|_r$ within the outside plastic region can be determined from Eq. (56) with initial values of stresses conditions at $r = r_{cs}$ instead of those at $r = a$.

(f) Fully critical-state phase

When the entire soil enters the critical state, Eq. (47) can be simplified as:

$$\Delta U\big|_r = \Delta U\big|_{r=a}^{cs} + \frac{kq_{cs}}{k+1}\ln\left[\frac{\exp(\gamma_a)-1}{\exp(\gamma)-1}\right] \tag{58}$$

where $\Delta U\big|_{r=a}^{cs} = p'_0 - \left[p'_{cs} + kq_{cs}/(k+1)\right]$.

4 Solution validation and parametric analysis

This section presents some selected results of cavity expansion and contraction curves under different loading/unloading programs. The following results were calculated with the critical state parameters relevant to London Clay ($\Gamma = 2.759$, $\lambda = 0.161$, $\kappa = 0.062$, $\varphi_{cs} = 22.75^{\circ}$ [22]), v=2.0 and μ=0.3. All the results are normalised by the undrained shear strength s_u, which can be obtained with $q_{cs} = 2s_u$ as:

$$s_u = 0.5Mp'_0\left(R_0 / r^*\right)^{\Lambda} \tag{59}$$

4.1 Cavity response under internal loading

Solutions for cavity expansion in an infinite soil mass under internal loading have been developed by Collins and Yu [22] and Mo and Yu [40] for the (original and modified) Cam-Clay and CASM models, respectively. While taking the surrounding soil as infinite (i.e. setting $a_0 / b_0 \propto 0$), the present solutions can reduce exactly to their solutions.

Taking the solution for the modified Cam-Clay model as an example, selected results for clay samples with different values of R_0 and b_0/a_0 are compared in Figs. 3-5 to show their effects to the cavity expansion response and associated stress distributions.

Fig. 3 shows that the present solution gave virtually the same results as Collins and Yu [22] while considering an infinite soil mass. For a finite soil mass under internal loading, the ratio of b_0/a_0 may greatly influence the cavity pressure-expansion response. For example, with an expansion level up to a/a_0=4, three typical pressure-expansion responses are shown in Fig. 3, including: (a) In an infinite soil mass, a limit cavity pressure is reached (typically at around a/a_0=2), and this value remains almost constant during afterwards expansions. (b) For a cavity embedded in an intermediate-thick soil mass, a maximum cavity pressure close to the aforementioned limit pressure is reached upon loading. However, the cavity pressure drops with afterwards expansions when the effect of the constant stresses at the outer boundary prevails. (c) For a thin hollow cylinder or spherical shell, the maximum cavity pressure that can be reached is much smaller than the limit pressure, and the cavity pressure drops after a local peak when the outside boundary effect is activated and eventually gets close to the outside radial confining pressure at sufficiently large deformations. Overall, the maximum cavity pressure that the surrounding soil can sustain may decrease significantly with a decreasing value of b_0/a_0. A limit value of b_0/a_0 exists, beyond which the cavity expansion response immunes from the outer boundary effect. The limit ratio of b_0/a_0 decreases with increases of the over-consolidation ratio, and the limit ratio for a spherical cavity is generally smaller than that for a cylindrical cavity.

The observed reduction in the total cavity pressure during expansion is further explained by plotting results of stress distributions in the soil (Figs. 4 and 5) and stress paths of soil at the inner wall (Fig. 6) for typical values of b_0/a_0 and the over-consolidation ratio. The results were calculated with expansions up to a/a_0=4. Note the peak and ultimate points in Fig. 6(c) and 6(d) correspond to the points at which the peak and ultimate values of the internal cavity pressure were reached in Fig. 3, respectively. For the cylindrical case, increments of the out-of-plane stress were calculated using $\Delta\sigma_z' = \nu(\Delta\sigma_r' + \Delta\sigma_0')$ according to the plane strain assumption [72]. It was shown that the outer boundary effect may alter the total stress path of a soil particle but applies no influence on the effective stress path, which is consistent with that has been observed by

Juran and Mahmoodzadegan [35] in undrained TWC tests. At a given deformation level, Figs. 4-6 show that the excess pore pressures generated throughout the hollow cylinder or spherical shell are typically smaller than that generated at the same radii in the corresponding case of an infinite soil mass when the outer boundary effect applies, and the reductions caused become larger for smaller values of b_0/a_0. This explains the specimen radius ratio (i.e. b_0/a_0) dependent behaviour that was observed in the cavity expansion curves of Fig. 3. Besides, the excess pore pressure generated at the inner cavity wall remains positive upon loading in normally consolidated soils, whereas it may become negative in heavily consolidated soils when the value of b_0/a_0 is sufficiently small. This is consistent with the experimental observations of Silvestri et al. [58] in laboratory pressuremeter tests with TWCs of undrained clay.

Fig. 6 also shows that, once the soil element enters the plastic state, the mean effective stress reduces gradually before resting on the CSL for soft clays (i.e. $R_0 < r^*$), and, in contrast, it increases with expansions for heavily overconsolidated clays (i.e. $R_0 > r^*$) until reaches the critical state value. Although the effective stress path varies with the soil model or the values of n and r^* used (e.g. Fig. 2) [22,40], it was found that the above conclusions about the effects of the b_0/a_0 value and the over-consolidation ratio to the cavity expansion response still validate for other models in Table 1. Therefore, results for other models are not presented here for brevity.

4.2 Cavity closure under external loading

In this subsection, the cavity closure response under external loading is discussed based on the results calculated using the solution for the CASM model (setting n=2 and r^*=2) with different values of the ratio of b_0/a_0 and the over-consolidation ratio. For illustration, stresses at both the inner and outer boundaries of a hollow cylinder or spherical shell are presented in Figs. 7-10, plotted against the volumetric strain of the inner cavity $(\Delta V / V_0)\big|_{r=a} = (a_0^{\,k+1} - a^{k+1}) / a_0^{\,k+1}$.

The soil mass moves inwards with increasing external pressure, while keeping the internal cavity pressure constant (Figs. 7-10). Initially, the total external pressure rises rapidly with cavity contractions; then the speed of the increase slows down, followed by a sharp increase when the inner cavity becomes very small or almost filled (for example, with $(\Delta V / V_0)\big|_{r=a}$ larger than 0.8 for a cylindrical cavity and 0.9 for a spherical cavity).

The external pressure required for compressing the soil to contract may decrease significantly with a decreasing value of b_0/a_0 when it is smaller than a limit value, and this disparity slightly varies with the deformation level. Similar to that observed in the previous cavity expansion analysis, the limit ratio of b_0/a_0, beyond which the boundary effect to the cavity closure response become negligible, is also closely related to the stress history and cavity shape in this loading program. The limit value of b_0/a_0 decreases with increases of the over-consolidation ratio and is generally smaller for a spherical shell than a hollow cylinder. For example, it is approximately 20 (Fig. 7) and 10 (Fig. 8) for a hollow cylinder and spherical shell of normally consolidated soil (i.e. R_0 =1.001), respectively, and the corresponding values while R_0 =4 are 10 (Fig. 9) and 5 (Fig. 10), respectively.

The effective stress state of soil is mainly dependent on the over-consolidation ratio and local deformation. Once the soil element enters the plastic state, the mean effective stress reduces gradually before resting on the CSL for soft clay, and, in contrast, it increases gradually to the critical state value for heavily overconsolidated clay (Figs. 7-10). With the same level of cavity contraction, the compatibility conditions of Eqs. (6) and (11) describe that the shear strain at the outer boundary becomes smaller for a thicker soil sample, which results in the observed difference in the effective stresses at $r = b$ in Figs. 7-10. For example, the soil at $r = b$ may always remain elastic in a sufficiently thick soil sample, whereas it yields plastically or enters the critical state easily while the thickness of the surrounding soil is very thin.

As the soil goes through the same effective stress path and the internal cavity pressure is kept constant in the external loading program, the stress path of soil particles at the inner wall of the cavity for different values of b_0/a_0 overlap in Figs. 7-10 (i.e. blue lines). Hence, at the same level of cavity contraction, the initial boundary values at $r = a$ for the integration of the excess pore pressure remain unchanged for different values of b_0/a_0. However, the difference in the effective stresses between at $r = a$ and $r = b$ becomes greater for a larger value of b_0/a_0. As a result, greater excess pore pressure will be generated at $r = b$ for a thicker soil cylinder or spherical shell according to Eq. (47), which leads to the increase of the total external pressure with the value of b_0/a_0 in Figs.7-10. Although slight decreases may occur in a very thin cylinder or spherical shell of stiff clays (e.g. Figs. 9d and 10d), during contractions the excess pore pressure at $r = b$ changes in a very similar way as the external cavity pressure.

4.3 Cavity contraction under internal unloading

For the prediction of soil behaviour around shallow tunnels, undrained solutions for a cavity in a finite soil under the internal unloading program were derived by Zhuang et al. [75], adopting the original and modified Cam-Clay models. To investigate the unloading behaviour of TWCs, these solutions are also included in this paper together with the solutions for the internal loading program and new solutions for the CASM model under internal unloading. To briefly show the effect of the most relevant parameters (e.g. the over-consolidation ratio and b_0/a_0 value) to unloading response, some results obtained with the solution for the CASM model (taking r^*=3 and n=2) are presented in this subsection. Detailed parametric studies into this problem with the Cam-Clay models refer to Zhuang et al. [75].

Considering the surrounding soil as infinite (i.e. setting $a_0 / b_0 \propto 0$), the present unloading solution for the CASM model reduces to the solution of Mo and Yu [39]. Therefore, they produced identical results in this special case (Fig. 11). From the comparison shown in Fig. 11, it can be concluded that: (a) The stability of the surrounding soil (e.g. evaluated by $(p_0 - p_{in}) / s_u$) [10]) may drop significantly with smaller values of b_0/a_0, and a spherical shell of soil has higher stability than a hollow cylinder, keeping other parameters the same. (b) A limit ratio of b_0/a_0 exists, beyond which the boundary effect is negligible. The limit radius ratio for a spherical shell of soil is smaller than that for a hollow cylinder, and it decreases slightly with the over-consolidation ratio. (c) The degree of unloading in pressure (i.e. $(p_0 - p_{in}) / p_0$) that the soil can sustain increases with the over-consolidation ratio (i.e. the cavity stability can be improved as R_0 (or OCR) increased). This is consistent with the experimental observations of wellbore instability in undrained clays that were reported by Abdulhadi et al. [2].

5 Prediction of soil behaviour in TWC tests

To demonstrate the relevance of the derived solutions for modelling soil behaviour in TWC tests, comparisons between predicted and measured results of cavity expansion and contraction curves under each loading/unloading program are presented in this section.

5.1 Prediction of pressuremeter curves in TWC tests

Cavity expansion tests in a triaxial cylinder cell or calibration chamber have been widely used to stimulate self-boring pressuremeter tests, and TWC apparatuses with a small outer-to-inner diameter ratio (i.e. b_0/a_0) of 2 to 20 were often used in the laboratory [1,6,26,33,34,58]. Fig. 3 showed that the undrained cavity expansion response may be greatly influenced by the outer constant-stress boundary while $b_0/a_0<20$. This has also been reported by Pyrah and Anderson [49] and Juran and Mahmoodzadegan [35], among others. In this subsection, a comparison between predicted and observed expansion curves for TWC tests reported by Frikha and Bouassida [26] is presented to validate the ability of the derived solutions on capturing the outer boundary effect (or b_0/a_0 effect) in the interpretation of laboratory pressuremeter tests.

A hollow cylinder cell of D_i=20mm, D_o=100mm and H_t/D_o=3 was used in the undrained expansion tests of Frikha and Bouassida [26]. Keeping the outer confining pressure constant, the hollow cylinder specimens were loaded by increasing the internal cavity pressure. This conforms to the defined internal loading program. Therefore, the TWC test is simulated as an undrained cylindrical cavity expansion process based on the derived solutions for the internal loading analysis. The CASM model is used to describe the stress-strain behaviour of the normally consolidated Speswhite kaolin that used in the tests. With reference to the soil parameters that were reported by Atkinson et al. [7] and Frikha and Bouassida [26], model parameters of CASM are calibrated by simulating the undrained triaxial compression tests that were conducted with the same soil as shown in Fig. 12. It gives: $\Gamma = 3.14$, $\lambda = 0.136$, $\kappa = 0.025$, $\varphi_{\mathrm{tc}} = 22.5^{\circ}$, $\mu = 0.3$, $n = 2$, and $r^* = 1.7 \sim 2.0$.

To account for the shear mode effect, $\varphi_{cs} = 1.2\varphi_{\mathrm{tc}}$ is taken in the cylindrical cavity expansion analysis [13]. For comparison, results without considering the shear mode effect (i.e. $\varphi_{cs} = \varphi_{\mathrm{tc}}$) or the boundary effect (i.e. setting $b_0 / a_0 \propto \infty$, corresponding to the infinite solutions) were also calculated. Predicted and observed expansion curves are compared by plotting the net total cavity pressures $(p_{\mathrm{in}} - p_0)$ against the cavity volumetric strain $(\Delta V / V_0)\big|_{r=a}$ in Fig. 13. From Fig. 13, it can be concluded that the present finite solution can accurately predict the pressuremeter curves of undrained TWC tests with due consideration of the boundary effect and the shear mode effect. Without considering the finite thickness of the TWCs of soil, the infinite solution significantly over-predicts the cavity pressure, and the over-prediction becomes more serious at larger cavity expansions. On the contrary, the required expansion pressure is under-estimated when the shear mode effect is neglected.

By plotting pressuremeter results in terms of cavity pressure against the logarithm of the volumetric strain, the plastic portion is almost a straight line (e.g. in the range of cavity strains between 5 and 15%) for tests performed in large containers or 'semi-infinite' field conditions, and the slope is often assumed to be equal to the undrained shear strength of the soil [21,28,38]. However, Fig. 14 shows that this method is not always suitable for the interpretation of laboratory pressuremeter tests in TWC apparatuses. An obvious reduction in strength is observed due to the boundary effect while b_0 / a_0 of the soil specimen is smaller than 20. Yu [70] gave a comprehensive review of various sources of inaccuracy that may exist in this simplified interpretation method, including effects of pressuremeter geometry, water drainage conditions, strain rate and disturbance during installation. The present study further demonstrates that attention should also be paid to the outer boundary effect while small-sized hollow cylinder cells are used in laboratory pressuremeter tests.

5.2 Contraction response under internal unloading and external loading

A series of TWC tests were performed by Abdulhadi [1] to investigate the wellbore instability problem in soils under either internal unloading (e.g. TWC1 and TWC3) or external loading (e.g. TWC2). Tests TWC1, TWC2 and TWC3 were chosen for the comparison here as they were performed in fully saturated, uniform, isotropically consolidated hollow cylinder specimens. The inner and outer diameters of the hollow cylinder specimen were 25mm and 76mm, respectively. The specimen height was 152mm, and it has been verified that this height to outer diameter ratio (H_t/D_o=2) produced a minimal impact on the borehole response [3], which fulfils the plane strain assumption. Reconstituted Boston blue clay (RBBC) was used in the tests. To determine the soil parameters in CASM, the triaxial compression test on isotropically consolidated RBBC that reported by Ladd [37] is simulated as shown in Fig. 15. It gives: $\Gamma = 2.671$, $\lambda = 0.184$, $\kappa = 0.01$, $\mu = 0.28$, $\varphi_{\mathrm{tc}} = 33.4^{\circ}$, $n = 1.5$, and $r^* = 2.1$. The soil parameters were determined by cross-referencing to the oedometric test data reported by Abdulhadi [1] and those summarised by Akl and Whittle [4]. These tests are simulated as a cylindrical cavity contraction process using the derived solutions. The same set of model parameters were used in the model predictions, and R_0=1.001 was taken as the soil specimens were normally consolidated.

Predicted and measured cavity contraction curves for tests performed under internal unloading and external loading are compared in Figs. 16 and 17, respectively. In tests TWC1 and TWC3, the soil cylinder contracts due to the internal unloading (Fig. 16). Instead, the specimen deforms inwards driven by the external compression in test TWC2 (Fig. 17). Compared to the experimental data, the theoretical solutions tend to underestimate soil stiffness during the initial contractions in both cases. A comparison between the idealised cavity contraction models and the experimental observations indicates that this discrepancy may be attributed to the following aspects. Firstly, it was observed that the pore pressures were not fully equilibrated across the width of the clay specimen with a loading or unloading rate of 10%/hour (approximately 80-90% equilibrated [2]). In other words, the applied pressures at the boundaries cannot transfer through the whole soil specimen immediately. Secondly, the predicted effective stress paths within soil slightly deviate from that occurred in the tests. Although RBBC has been used at MIT (Massachusetts Institute of Technology) for over 50 years, the raw Boston clay, the re-sedimentation procedure and consolidation pressures during sample preparations in the triaxial compression tests of Ladd [37] and the TWC tests of Abdulhadi [1] were not exactly the same, which may lead to some deviations in the stress-strain behaviour. Moreover, the inherent boundary effect caused during sample preparation and the rate dependence in soil behaviour, which are ignored in the present model, may also result in differences between physical tests and theoretical models more or less [2]. It seems that the overall influences of the above factors produced relatively greater influences on the initial contraction response as the predicted and measured results are in close agreement at relatively large deformations (e.g. the steady contraction stage). Nevertheless, the comparisons in Figs. 16 and 17 indicate that, with due consideration of the shear mode effect, the predicted cavity contraction curves under either internal unloading or external loading are basically consistent with those measured in the tests, in particular, at the steady contraction stage (or the most vulnerable stage) which is of great concern for the borehole instability analysis. If the boundary effect is ignored (e.g. in the infinite solution), the soil stability under internal unloading could be significantly over-predicted (Fig. 16).

Tests TWC1 and TWC3 were performed with the same initial confining pressures. It is interesting to note these two tests show similar soil stability results if evaluated in terms of $(p_{\text{out}} - p_{\text{in}}) / s_u$. However, the total stress paths or excess pore pressures are essentially different in these two cases as also highlighted by Abdulhadi [1]. In addition, the results in Figs. 16 and 17 indicate that the back-calculated critical state friction angle φ_{cs} from the test under internal unloading (e.g. TWC1) is slightly smaller than that based on the test under external loading (e.g. TWC1). This minor difference might be caused by the loading path effect, but this needs to be justified with more experimental evidence.

It should be pointed out that, in previous TWC tests, the pore pressure is mostly measured at the axial ends and only assumed average values across the width of the specimen are available. Therefore, only the total stresses are compared in the above cases. As a consequence, possible influences of local consolidation and rate-dependent redistribution of the pore pressure cannot be evaluated from these experimental results. These effects might be significant, in particular, for tests with relatively thick soil samples, and direct detection of them could be very useful for the investigation on relevant soil properties (e.g. hydraulic properties). Therefore, it is believed that TWC test apparatus equipped with more advanced imaging techniques such as X-ray Computed Tomography [36,41,59] can offer additional insight into the soil behaviour involved due to its ability to probe the 3D in situ soil porous architecture at high resolutions (i.e. 1 μm).

6 | Conclusions

We have presented a general solution procedure for undrained loading and unloading analyses of both cylindrical and spherical cavities embedded in soils with a finite radial extent, which is applicable to many two-invariant critical state soil models. Three stress-controlled loading programs (internal loading, internal unloading and external loading) that are commonly used in TWC tests are considered. Following the proposed procedure, a set of large strain analytical/semi-analytical cavity expansion and contraction solutions are derived for several critical state soil models, which can provide valuable benchmark for verifying various numerical programs. The derived solutions are used to investigate the boundary effect (or specimen size effect) to the cavity expansion and contraction responses. It is shown that a limit value of b_0/a_0 exists in each loading/unloading program, below which the boundary effect could lead to significant reductions in the degree of loading or unloading that the surrounding soil can sustain. Although the limit value of b_0/a_0 may vary with the over-consolidation ratio and the cavity deformation level, it was found that, in general, $b_0 / a_0 \geq 20$ is a minimum practical requirement to remove the boundary effect in common TWC tests under undrained conditions, and this value is much smaller for a spherical shell of soil (approximately $b_0 / a_0 \geq 10$).

Using the published results of several TWC tests under different stress-controlled loading/unloading programs in the literature, comparisons between predicted and measured cavity expansion and contraction curves are made. Overall, the theoretical predictions show satisfactory agreement with the experimental data. The results of these comparisons suggest that the proposed cylindrical solutions are able to capture the boundary effect that is commonly observed in undrained TWC tests under the considered three loading/unloading programs. This is essential for the interpretation of laboratory TWC tests. Inversely, the finite cavity expansion and contraction solutions may be calibrated or validated with relevant TWC tests which require less energy, time and space than site tests. Then setting $b_0 / a_0 \propto \infty$, the calibrated solutions can be used to simulate field pressuremeter tests and investigate the in-situ wellbore instability problem as the infinite cavity expansion or contraction solutions often did [14,18,71].

Acknowledgements

The authors would like to acknowledge the Open Research Fund of the State Key Laboratory for Geomechanics and Deep Underground Engineering China University of Mining and Technology (SKLGDUEK1802) and the International Mobility Fund from the University of Leeds. The first author also acknowledges the support of the 'Taishan' Scholar Program of Shandong Province, China (No. tsqn201909016) and the 'Qilu' Scholar Program of Shandong University.

References

1. Abdulhadi NO (2009) An experimental investigation into the stress-dependent mechanical behavior of cohesive soil with application to wellbore instability. PhD thesis, Massachusetts Institute of Technology, Cambridge, MA, USA
2. Abdulhadi NO, Germaine JT, Whittle AJ (2010) Experimental study of wellbore instability in clays. Journal of Geotechnical and Geoenvironmental Engineering 137 (8):766-776
3. Abdulhadi NO, Germaine JT, Whittle AJ (2011) Thick-walled cylinder testing of clays for the study of wellbore instability. Geotechnical Testing Journal 34 (6):746-754
4. Akl SA, Whittle AJ (2016) Validation of soil models for wellbore stability in ductile formations using laboratory TWC tests. Journal of Geotechnical and Geoenvironmental Engineering 143 (2):04016095
5. Alsiny A, Vardoulakis I, Drescher A (1992) Deformation localization in cavity inflation experiments on dry sand. Geotechnique 42 (3):395-410
6. Anderson WF, Pyrah IC, Ali FH (1987) Rate effects in pressuremeter tests in clays. Journal of Geotechnical Engineering 113 (11):1344-1358
7. Atkinson J, Richardson D, Robinson P (1987) Compression and extension of K 0 normally consolidated kaolin clay. Journal of Geotechnical Engineering 113 (12):1468-1482
8. Au AS, Yeung AT, Soga K (2006) Pressure-controlled cavity expansion in clay. Canadian Geotechnical Journal 43 (7):714-725
9. Augarde CE, Lyamin AV, Sloan SW (2003) Prediction of undrained sinkhole collapse. Journal of Geotechnical and Geoenvironmental Engineering 129 (3):197-205
10. Broms BB, Bennermark H (1967) Stability of clay at vertical openings. Journal of Soil Mechanics & Foundations Division 93 (1):71-94
11. Carter JP (1978) CAMFE, a computer program for the analysis of a cylindrical cavity expansion in soil. Report CUED/C–Soils TR52, Department of Engineering, University of Cambridge, Cambridge, UK
12. Carter JP, Booker JR, Yeung SK (1986) Cavity expansion in cohesive frictional soils. Geotechnique 36 (3):349-358
13. Chang M-F, Teh CI, Cao L (1999) Critical state strength parameters of saturated clays from the modified Cam clay model. Canadian Geotechnical Journal 36 (5):876-890

14. Charlez PA, Roatesi S (1999) A fully analytical solution of the wellbore stability problem under undrained conditions using a linearised Cam-Clay model. Oil & Gas Science and Technology 54 (5):551-563

15. Chen SL, Abousleiman YN (2012) Exact undrained elasto-plastic solution for cylindrical cavity expansion in modified Cam Clay soil. Geotechnique 62 (5):447-456

16. Chen SL, Abousleiman YN (2013) Exact drained solution for cylindrical cavity expansion in modified Cam Clay soil. Geotechnique 63 (6):510-517

17. Chen SL, Abousleiman YN (2016) Drained and undrained analyses of cylindrical cavity contractions by bounding surface plasticity. Canadian Geotechnical Journal 53 (9):1398-1411

18. Chen SL, Abousleiman YN (2017) Wellbore stability analysis using strain hardening and/or softening plasticity models. International Journal of Rock Mechanics and Mining Sciences 93:260-268

19. Cheng Y, Yang H-W (2019) Exact solution for drained spherical cavity expansion in saturated soils of finite radial extent. International Journal for Numerical and Analytical Methods in Geomechanics 43:1594–1611. doi:doi: org/10.1002/nag.2924

20. Cheng Y, Yang H-W, Sun DA (2018) Cavity expansion in unsaturated soils of finite radial extent. Computers and Geotechnics 102:216-228

21. Clarke BG (1993) The interpretation of self-boring pressuremeter tests to produce design parameters. Paper presented at the Predictive soil mechanics: Proceedings of the Wroth Memorial Symposium, London, UK,

22. Collins IF, Yu HS (1996) Undrained cavity expansions in critical state soils. International Journal for Numerical and Analytical Methods in Geomechanics 20 (7):489-516

23. Doreau-Malioche J, Combe G, Viggiani G, Toni J (2018) Shaft friction changes for cyclically loaded displacement piles: an X-ray investigation. Géotechnique Letters 8 (1):66-72

24. Durban D, Papanastasiou P (1997) Cylindrical cavity expansion and contraction in pressure sensitive geomaterials. Acta mechanica 122:99-122

25. Fahey M (1986) Expansion of a thick cylinder of sand: a laboratory simulation of the pressuremeter test. Geotechnique 36 (3):397-424

26. Frikha W, Bouassida M (2015) Comparison between results of triaxial shear test and expansion of cavity in hollow cylinder. Paper presented at the ISP7-Pressio 2015, Hammaet, Tunisia,
27. Ghionna VN, Jamiolkowski M A critical appraisal of calibration chamber testing of sands. In: the First International Symposium on Calibration Chamber Testing, Potsdam, New York, 1991. Elsevier, pp 13-40
28. Gibson RE, Anderson WF (1961) In situ measurement of soil properties with the pressuremeter. Civil Engineering and Public Works Review 56 (658):615-618
29. Goodarzi M, Stähler F, Kreiter S, Rouainia M, Kluger M, Mörz T (2018) Numerical simulation of cone penetration test in a small-volume calibration chamber: The effect of boundary conditions. Paper presented at the 4th International Symposium on Cone Penetration Testing (CPT 2018), Delft, the Netherlands,
30. Hill R (1950) The mathematical theory of plasticity. Oxford University Press, London
31. Huang AB, Holtz RD, Chameau JL (1991) Laboratory study of pressuremeter tests in clays. Journal of Geotechnical Engineering 117 (10):1549-1567
32. Hughes JMO, Wroth CP, Windle D (1977) Pressuremeter tests in sands. Geotechnique 27 (4):455-477
33. Jewell R, Fahey M, Wroth C (1980) Laboratory studies of the pressuremeter test in sand. Geotechnique 30 (4):507-531
34. Juran I, BenSaid M (1987) Cavity expansion tests in a hollow cylinder cell. Geotechnical Testing Journal 10 (4):203-212
35. Juran I, Mahmoodzadegan B (1990) Laboratory measurement of lateral stress induced by a cavity expansion in a hollow cylinder cell. Transportation Research Record (1278):204-214
36. Labiouse V, Sauthier C, You S (2014) Hollow cylinder simulation experiments of galleries in boom clay formation. Rock Mechanics and Rock Engineering 47 (1):43-55
37. Ladd C (1965) Stress-strain behaviour of anisotropically consolidated clays during undrained shear. Paper presented at the Proceedings of the 6th International Conference on Soil Mechanics and Foundation Engineering, Montréal,
38. Mair RJ, Wood DM (1987) Pressuremeter testing: methods and interpretation. CIRIA-Butterworths, London, UK

39. Mo PQ, Yu HS (2017) Undrained Cavity-Contraction Analysis for Prediction of Soil Behavior around Tunnels. International Journal of Geomechanics 17 (5):04016121-04016121-04016110. doi:DOI: 10.1061/(ASCE)GM.1943-5622.0000816.

40. Mo PQ, Yu HS (2017) Undrained cavity expansion analysis with a unified state parameter model for clay and sand. Geotechnique 67 (6):503-515. doi:DOI: 10.1680/jgeot.15.P.261.

41. Mooney SJ (2002) Three - dimensional visualization and quantification of soil macroporosity and water flow patterns using computed tomography. Soil Use and Management 18 (2):142-151

42. Palmer AC (1971) Undrained plane-strain expansion of a cylindrical cavity in clay: a simple interpretation of the pressuremeter test. Division of Engineering, Brown University, Providence, RI, USA

43. Paniagua P, Andò E, Silva M, Emdal A, Nordal S, Viggiani G (2013) Soil deformation around a penetrating cone in silt. Géotechnique Letters 3 (4):185-191

44. Papamichos E (2010) Borehole failure analysis in a sandstone under anisotropic stresses. International Journal for Numerical and Analytical Methods in Geomechanics 34 (6):581-603

45. Papamichos E, Tronvoll J, Skjærstein A, Unander TE (2010) Hole stability of Red Wildmoor sandstone under anisotropic stresses and sand production criterion. Journal of Petroleum Science and Engineering 72 (1-2):78-92

46. Perić D, Ayari MA (2002) On the analytical solutions for the three-invariant Cam clay model. International Journal of Plasticity 18 (8):1061-1082

47. Pournaghiazar M, Russell AR, Khalili N (2012) Linking cone penetration resistances measured in calibration chambers and the field. Géotechnique Letters 2 (2):29-35

48. Pournaghiazar M, Russell AR, Khalili N (2013) Drained cavity expansions in soils of finite radial extent subjected to two boundary conditions. International Journal for Numerical and Analytical Methods in Geomechanics 37 (4):331-352

49. Pyrah IC, Anderson WF (1990) Numerical assessment of self-boring pressuremeter tests in a clay calibration chamber. Paper presented at the Proceedings of the Third International Symposium on Pressuremeters, London, UK,

50. Roscoe KH, Burland JB (1968) On the generalized stress-strain behaviour of wet clay. In: Heymann G, Leckie FA (eds) Engineering Plasticity. Cambridge University Press, London, UK, pp 535-609

51. Roscoe KH, Schofield AN (1963) Mechanical behaviour of an idealized'wet'clay. Paper presented at the Proceedings of the 3rd European Conference on Soil Mechanics and Foundation Engineering,
52. Roscoe KH, Schofield AN, Wroth CP (1958) On the yielding of soils. Geotechnique 8 (1):22-53
53. Salgado R, Mitchell JK, Jamiolkowski M (1997) Cavity expansion and penetration resistance in sand. Journal of Geotechnical and Geoenvironmental Engineering 123 (4):344-354
54. Salgado R, Mitchell JK, Jamiolkowski M (1998) Calibration chamber size effects on penetration resistance in sand. Journal of Geotechnical and Geoenvironmental Engineering 124 (9):878-888
55. Schnaid F, Houlsby G (1991) An assessment of chamber size effects in the calibration of in situ tests in sand. Geotechnique 41 (3):437-445
56. Sheng D, Sloan SW, Yu HS (2000) Aspects of finite element implementation of critical state models. Computational Mechanics 26 (2):185-196
57. Silvestri V (1998) On the determination of the stress-strain curve of clay from the undrained plane-strain expansion of hollow cylinders: a long-forgotten method. Canadian Geotechnical Journal 35 (2):360-363
58. Silvestri V, Diab R, Ducharme A (2005) Development of a new hollow cylinder triaxial apparatus for the study of expansion tests in clay. Geotechnical Testing Journal 28 (3):231-239
59. Tracy SR, Daly KR, Sturrock CJ, Crout NM, Mooney SJ, Roose T (2015) Three - dimensional quantification of soil hydraulic properties using X - ray Computed Tomography and image - based modeling. Water Resources Research 51 (2):1006-1022
60. van Nes JHG (2004) Application of computerized tomography to investigate strain fields caused by cone penetration in sand. Master Dissertation, Delft University of Technology, Delft, the Netherlands
61. Vrakas A (2016) A rigorous semi - analytical solution for undrained cylindrical cavity expansion in critical state soils. International Journal for Numerical and Analytical Methods in Geomechanics 40 (15):2137-2160

62. Vrakas A, Anagnostou G (2015) Finite strain elastoplastic solutions for the undrained ground response curve in tunnelling. International Journal for Numerical and Analytical Methods in Geomechanics 39 (7):738-761
63. Wang CL, Zhou H, Liu HL, Ding XM (2019) Analysis of undrained spherical cavity expansion in modified Cam Clay of finite radial extent. European Journal of Environmental and Civil Engineering:1-12. doi:org/10.1080/19648189.2019.1687015
64. Wood DM (1990) Soil behaviour and critical state soil mechanics. Cambridge University Press, Cambridge, UK
65. Wroth CP (1984) The interpretation of in situ soil tests. Geotechnique 34 (4):449-489
66. Yu HS (1992) Expansion of a thick cylinder of soils. Computers and Geotechnics 14 (1):21-41
67. Yu HS (1993) Finite elastoplastic deformation of an internally pressurized hollow sphere. Acta Mechaniea Solida Sinica (English Edition) 6 (1):81–97
68. Yu HS (1998) CASM: A unified state parameter model for clay and sand. International Journal for Numerical and Analytical Methods in Geomechanics 22 (8):621-653
69. Yu HS (2000) Cavity expansion methods in geomechanics. Kluwer Academic Publishers, Dordrecht, the Netherlands
70. Yu HS (2006) The First James K. Mitchell Lecture: In situ soil testing: from mechanics to interpretation. Geomechanics and Geoengineering: An International Journal 1 (3):165-195
71. Yu HS, Collins IF (1998) Analysis of self-boring pressuremeter tests in overconsolidated clays. Geotechnique 48 (5):689-693
72. Yu HS, Houlsby GT (1991) Finite cavity expansion in dilatant soils: loading analysis. Geotechnique 41 (2):173-183
73. Yu HS, Rowe RK (1999) Plasticity solutions for soil behaviour around contracting cavities and tunnels. International Journal for Numerical and Analytical Methods in Geomechanics 23 (12):1245-1279
74. Zervos A, Papanastasiou P, Vardoulakis I (2001) Modelling of localisation and scale effect in thick-walled cylinders with gradient elastoplasticity. International Journal of Solids and Structures 38 (30):5081-5095

75. Zhuang PZ, Yang H, Yu HS, Fuentes R, Song XG (2019) Plasticity solutions for predictions of undrained stability and ground deformation of shallow tunnels in clay. Tunnelling and Underground Space Technology:(under review)

Figure captions

Fig.1. Schematic of a thick-walled cylinder.

Fig.2. Example yield surfaces of Cam-Clay models and CASM.

Fig.3. Total pressure and excess pore pressure at the inner cavity of modified Cam clay: (a) cylindrical solution with R_0=1.001; (b) spherical solution with R_0=1.001; (c) cylindrical solution with R_0=4; (d) spherical solution with R_0=4; (e) cylindrical solution with R_0=16; (f) spherical solution with R_0=16.

Fig.4. Stress distribution in modified Cam clay with R_0=1.001: (a) cylindrical model in an infinite soil mass; (b) spherical model in an infinite soil mass; (c) cylindrical model with small values of b_0/a_0; (d) spherical model with small values of b_0/a_0.

Fig.5. Stress distribution in modified Cam clay with R_0=16: (a) cylindrical model in an infinite soil mass; (b) spherical model in an infinite soil mass; (c) cylindrical model with small values of b_0/a_0; (d) spherical model with small values of b_0/a_0.

Fig.6. Typical stress paths in modified Cam clay: (a) cylindrical model with b_0/a_0=1000; (b) spherical model with b_0/a_0=1000; (c) cylindrical model with b_0/a_0=2; (d) spherical model with b_0/a_0=2.

Fig.7. A thick-walled cylinder of normally consolidated London clay (R_0=1.001) under external loading.

Fig.8. A spherical shell of normally consolidated London clay (R_0=1.001) under external loading.

Fig.9. A thick-walled cylinder cavity of stiff London clay (R_0=4) under external loading.

Fig.10. A spherical shell of stiff London clay (R_0=4) under external loading.

Fig.11. Cavity contraction curves under internal unloading: (a) and (c) cylindrical model; (b) and (d) spherical model.

Fig.12. Model prediction for undrained triaxial compression tests with soft Speswhite kaolin.

Fig.13. Predicted and measured cavity expansion curves in a thick-walled cylinder of kaolin clay.

Fig.14. Pressuremeter curves with different values of b_0/a_0 (Speswhite kaolin).

Fig.15. Model prediction for an undrained triaxial compression test on isotropically consolidated RBBC.

Fig.16. Predicted and measured cavity contraction curves in thick-walled cylinders of RBBC under internal unloading.

Fig.17. Predicted and measured cavity contraction curves in a thick-walled cylinder of RBBC under external loading.

Notation

p_{a} , p_{in} , p_{out}	axial stress, internal and external radial pressures
ς	$\varsigma = 1$ for loading and $\varsigma = -1$ for unloading
k	$k = 1$ for a cylindrical cavity and $k = 2$ for a spherical cavity
r, θ, z	coordinates of the cylindrical coordinate system
r, θ, φ	coordinates of the spherical coordinate system
r_0	initial value of the radial co-ordinate r
p' , q	mean effective stress and deviatoric stress
p'_{cs} , q_{cs}	mean effective stress and deviatoric stress at the critical state
p	mean total pressure
p_0 , p'_0	initial values of p and p'
U , U_0 , ΔU	total, initial ambient, excess pore pressures
$\Delta U\|_{r=a}$, $\Delta U\|_{r=b}$	excess pore pressures at $r = a$ and at $r = b$
$\Delta U\|_{r=a}$, $\Delta U\|_{r=b}$	excess pore pressures at $r = c$ and at $r = r_{cs}$
σ'_r , σ'_θ	effective radial and circumferential stresses
σ_r , σ_θ	total radial and circumferential stresses
ε_r , ε_θ	radial and circumferential strains
δ , γ	volumetric and shear strains
a_0, a ; b_0, b ; c_0, c	initial and current radii of the inner cavity wall, the outer cavity wall, the elastic-plastic boundary
r_{cs}	radius of the plastic-critical state boundary
p'_a , q_a	mean effective and shear stresses at $r = a$
p'_b , q_b	mean effective and shear stresses at $r = b$
γ_a , γ_b	shear strains at $r = a$ and at $r = b$
γ_{ep} , q_{ep}	shear strain and shear stress at the state just enters plastic yielding
K , G	instantaneous bulk and shear moduli with initial values of K_0 and G_0
M	the slope of the CSL in the p' - q space
λ	slope of the normally compression line
Γ	the value of v on the CSL at $p' = 1\mathrm{kPa}$

v, μ	specific volume and Poisson's ratio of soil
κ	slope of the swelling line
Λ	plastic volumetric strain ratio, equals $(\lambda-\kappa)/\lambda$
R_0	isotropic over-consolidation ratio, defines as p'_{y0}/p'_0
n, r^*	stress-state coefficient and spacing ratio in CASM
p'_y, p'_{y0}	preconsolidation pressure and its initial value
s_u	undrained shear strength of soil
η, η_{ep}	stress ratio and its value at the elastic-plastic boundary
φ_{cs}	critical state friction angle, Hvorslev friction angle
φ_{tc}	critical state friction angle under triaxial compression and plane strain
$\Delta V/V_0$	cavity volumetric strain

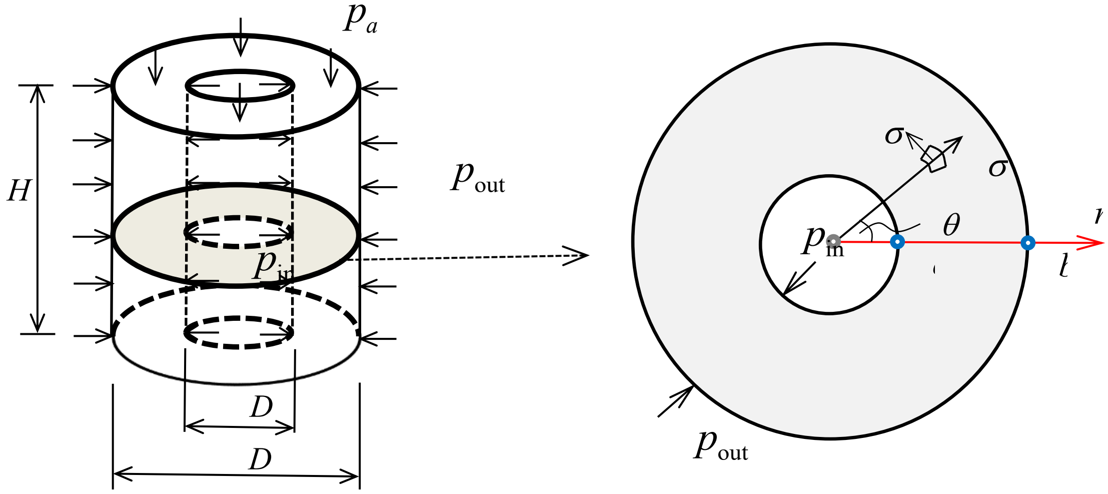

Fig 1 Schematic of a thick-walled cylinder

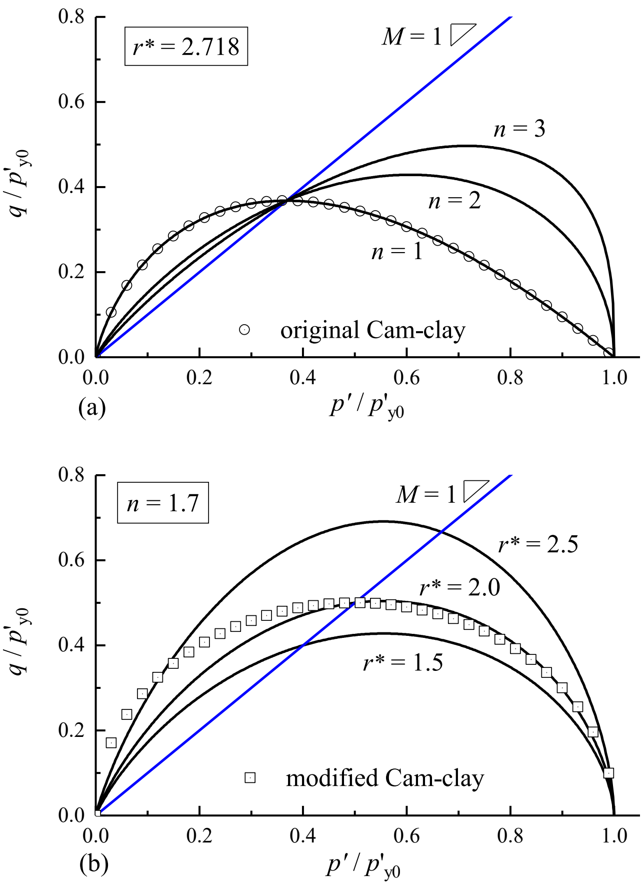

Fig 2 Example yield surfaces of Cam-clay models and CASM.

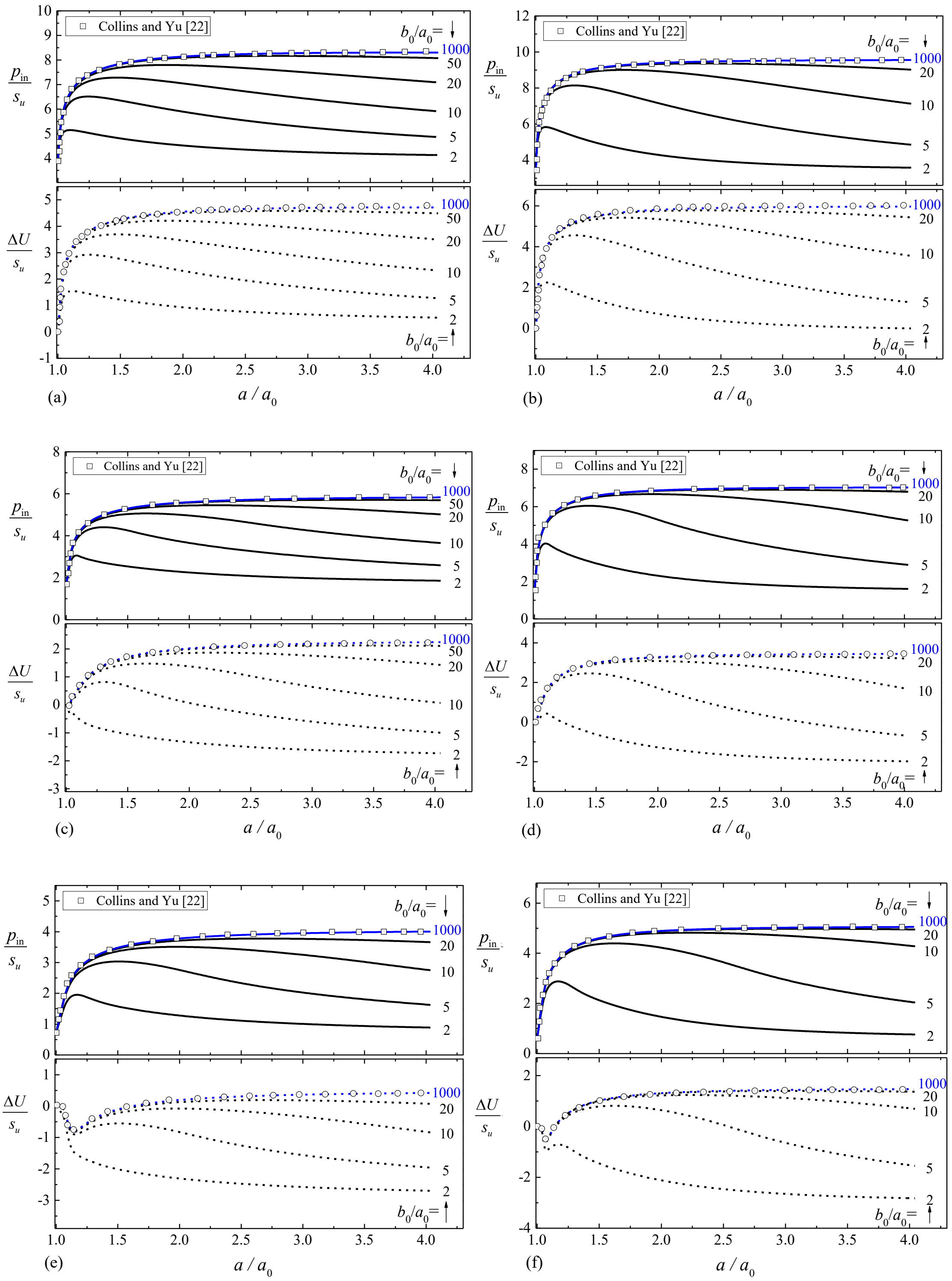

Fig. 3. Total pressure and excess pore pressure at the inner cavity of modified Cam clay: (a) cylindrical solution with R_0=1.001; (b) spherical solution with R_0=1.001; (c) cylindrical solution with R_0=4; (d) spherical solution with R_0=4; (e) cylindrical solution with R_0=16; (f) spherical solution with R_0=16.

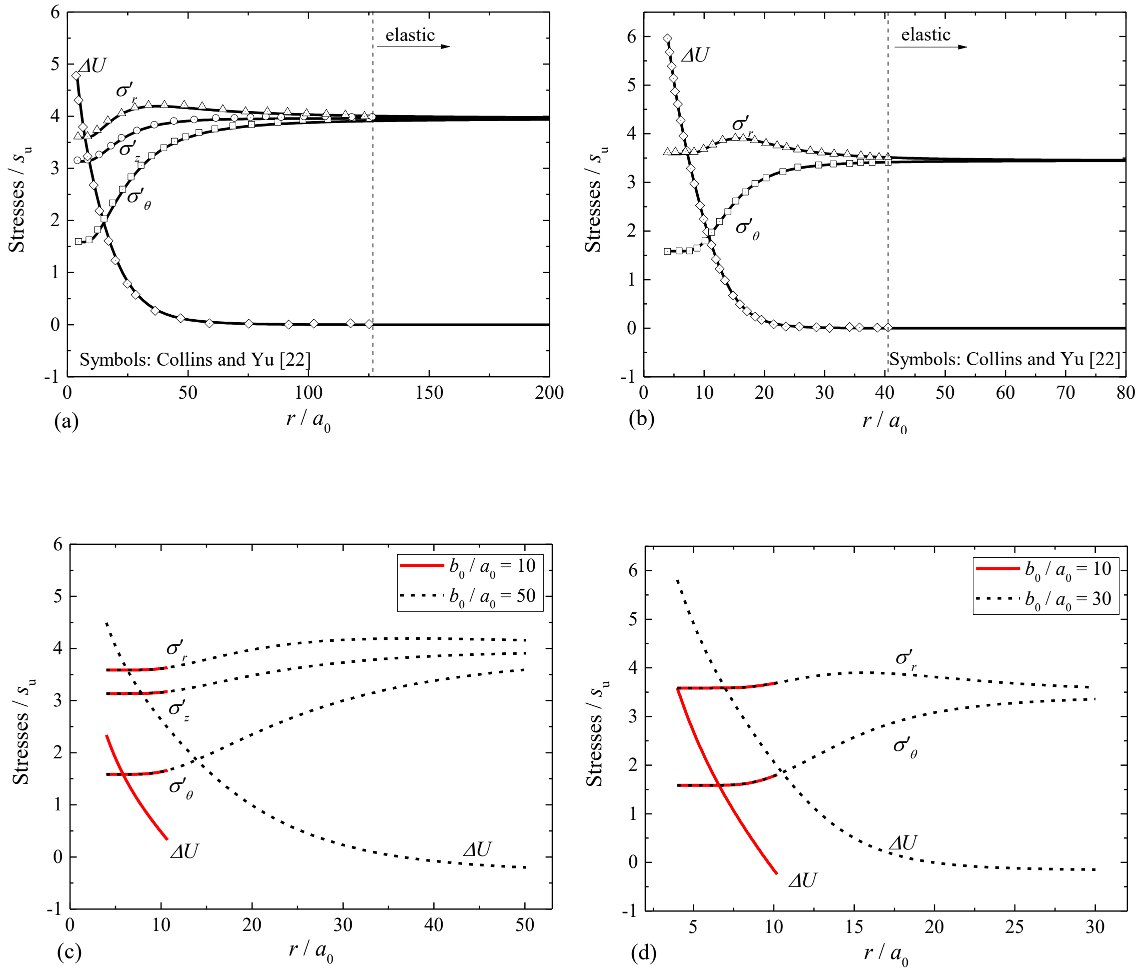

Fig. 4. Stress distribution in modified Cam clay with R_0=1.001: (a) cylindrical model in an infinite soil mass; (b) spherical model in an infinite soil mass; (c) cylindrical model with small values of b_0/a_0; (d) spherical model with small values of b_0/a_0.

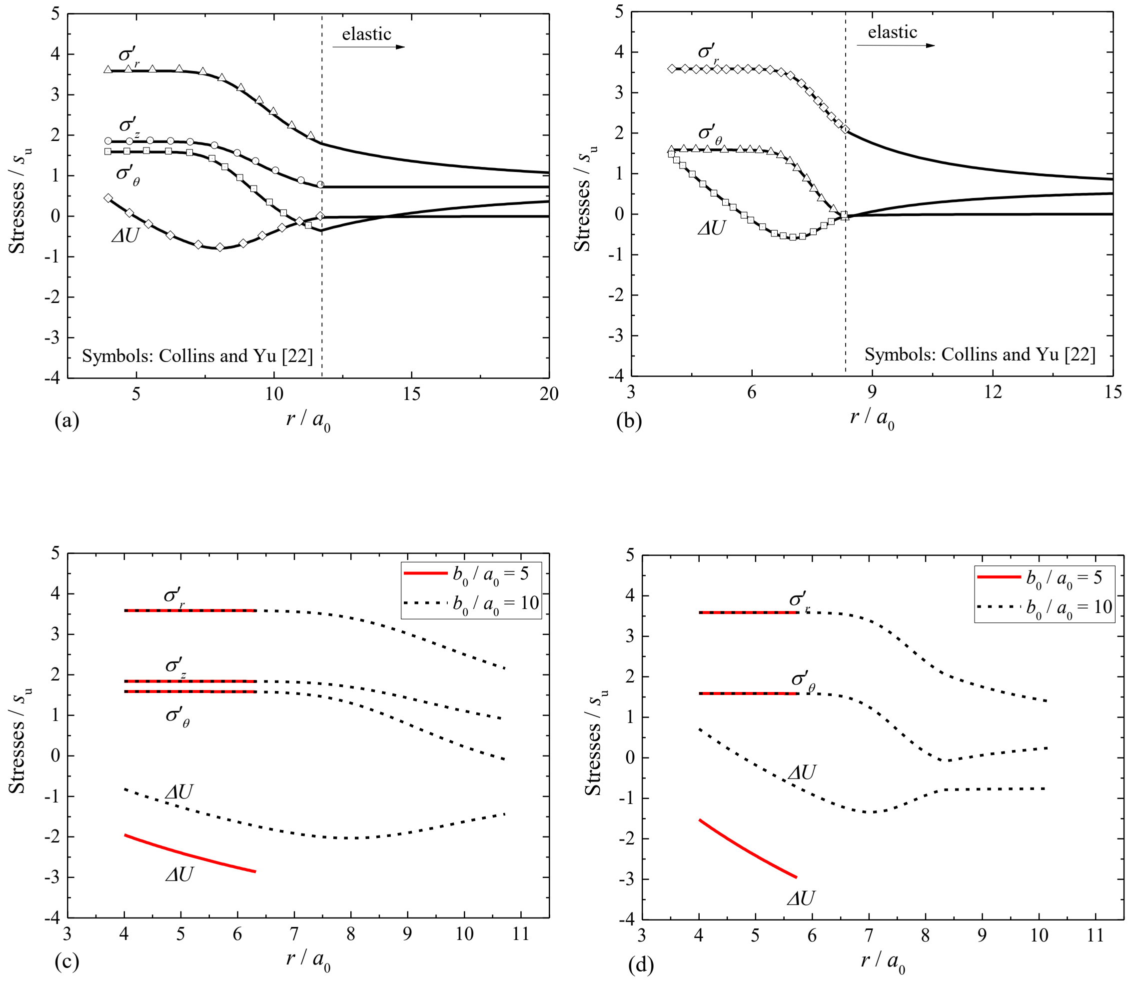

Fig. 5. Stress distribution in modified Cam clay with R_0=16: (a) cylindrical model in an infinite soil mass; (b) spherical model in an infinite soil mass; (c) cylindrical model with small values of b_0/a_0; (d) spherical model with small values of b_0/a_0.

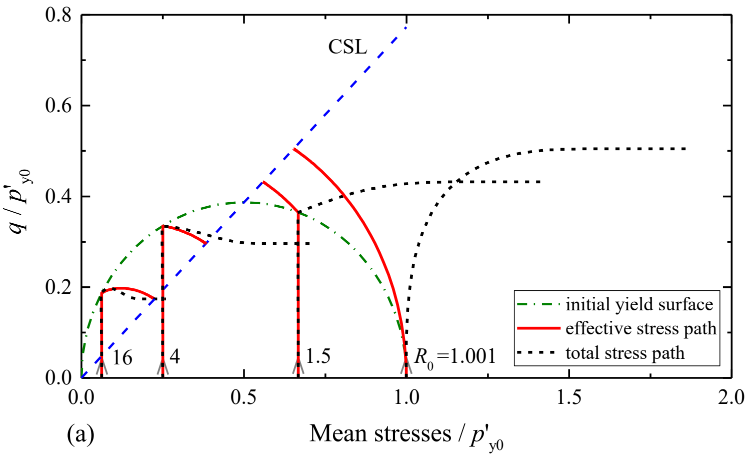

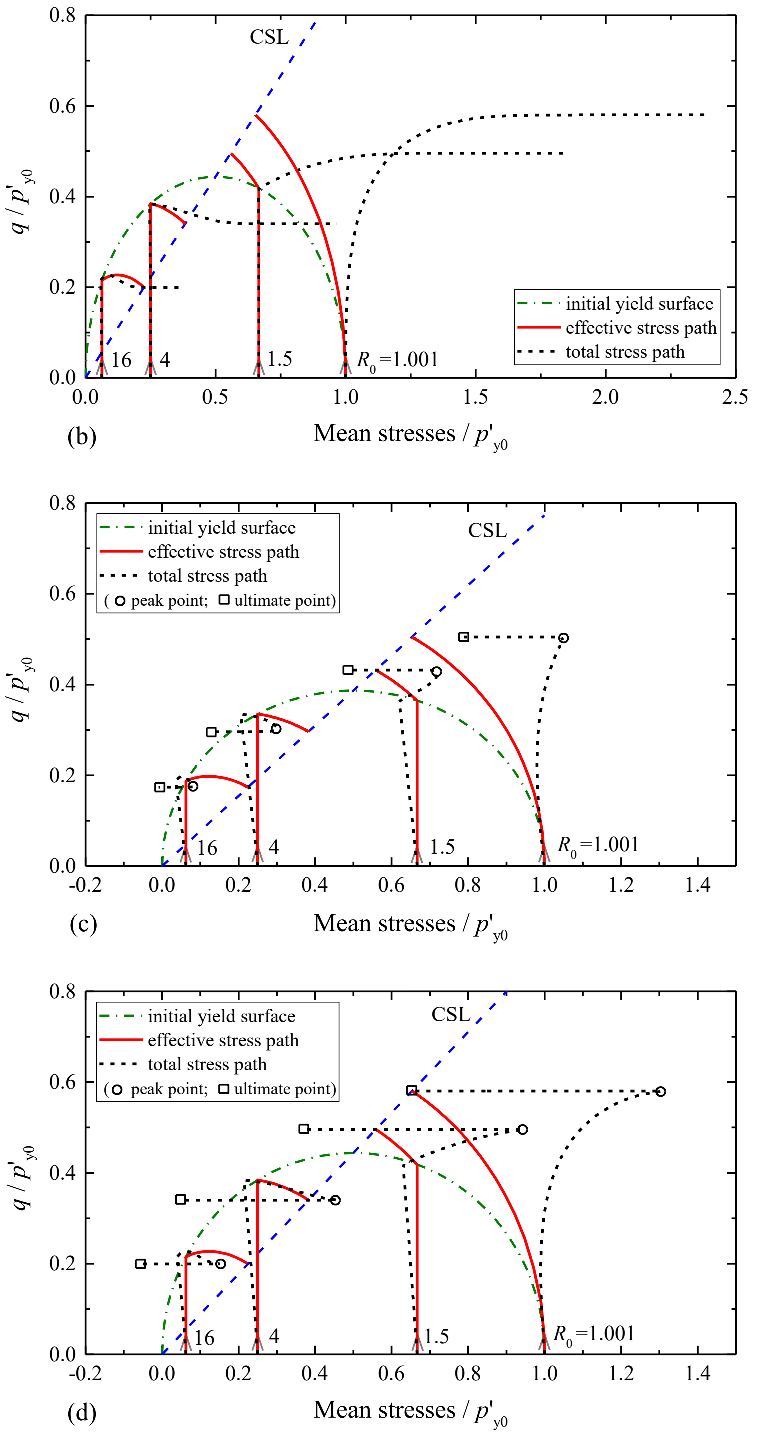

Fig. 6. Typical stress paths in modified Cam clay: (a) cylindrical model with b_0/a_0=1000; (b) spherical model with b_0/a_0=1000; (c) cylindrical model with b_0/a_0=2; (d) spherical model with b_0/a_0=2.

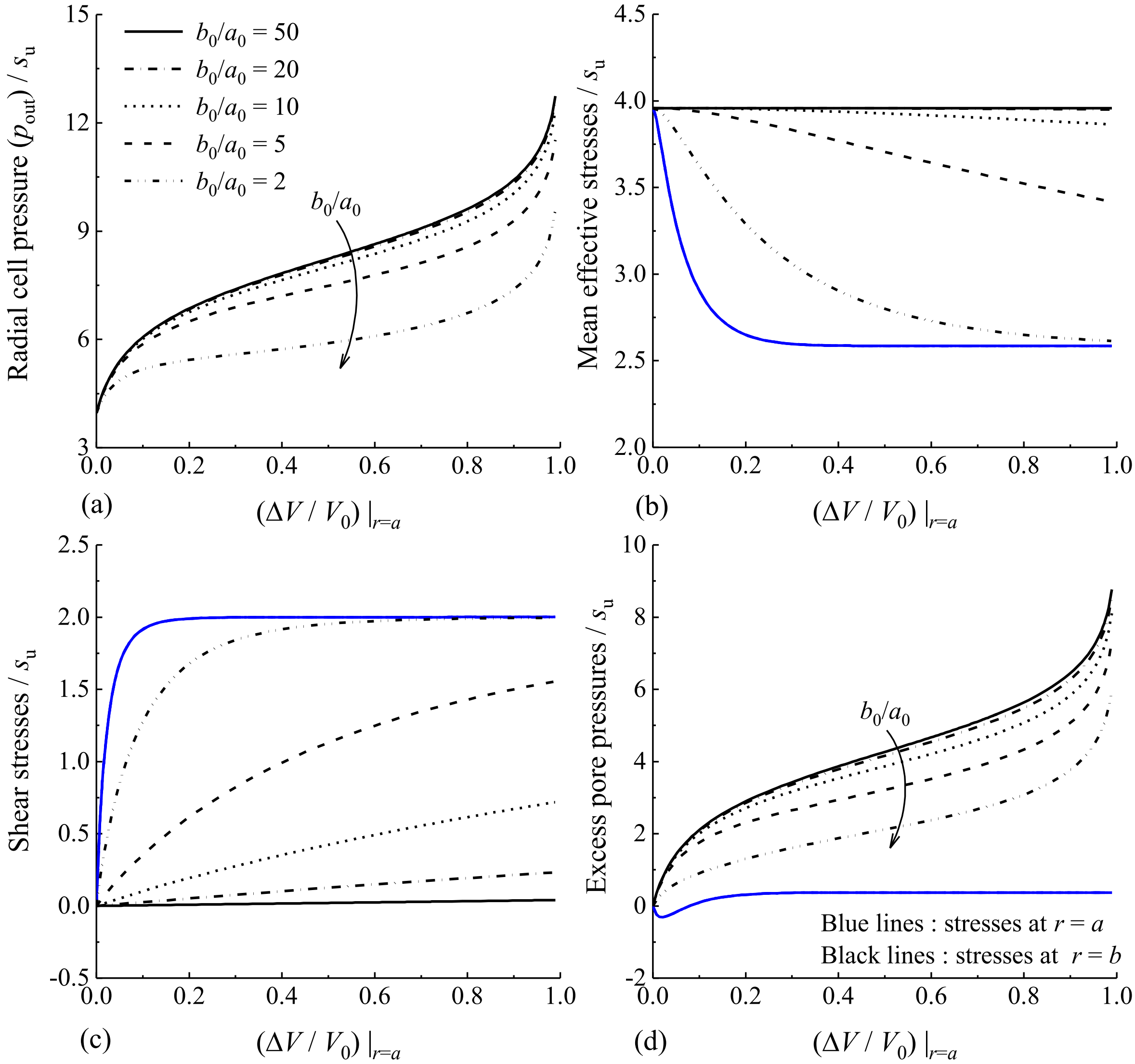

Fig 7. A thick-walled cylinder of normally consolidated London clay (R_0=1.001) under external loading.

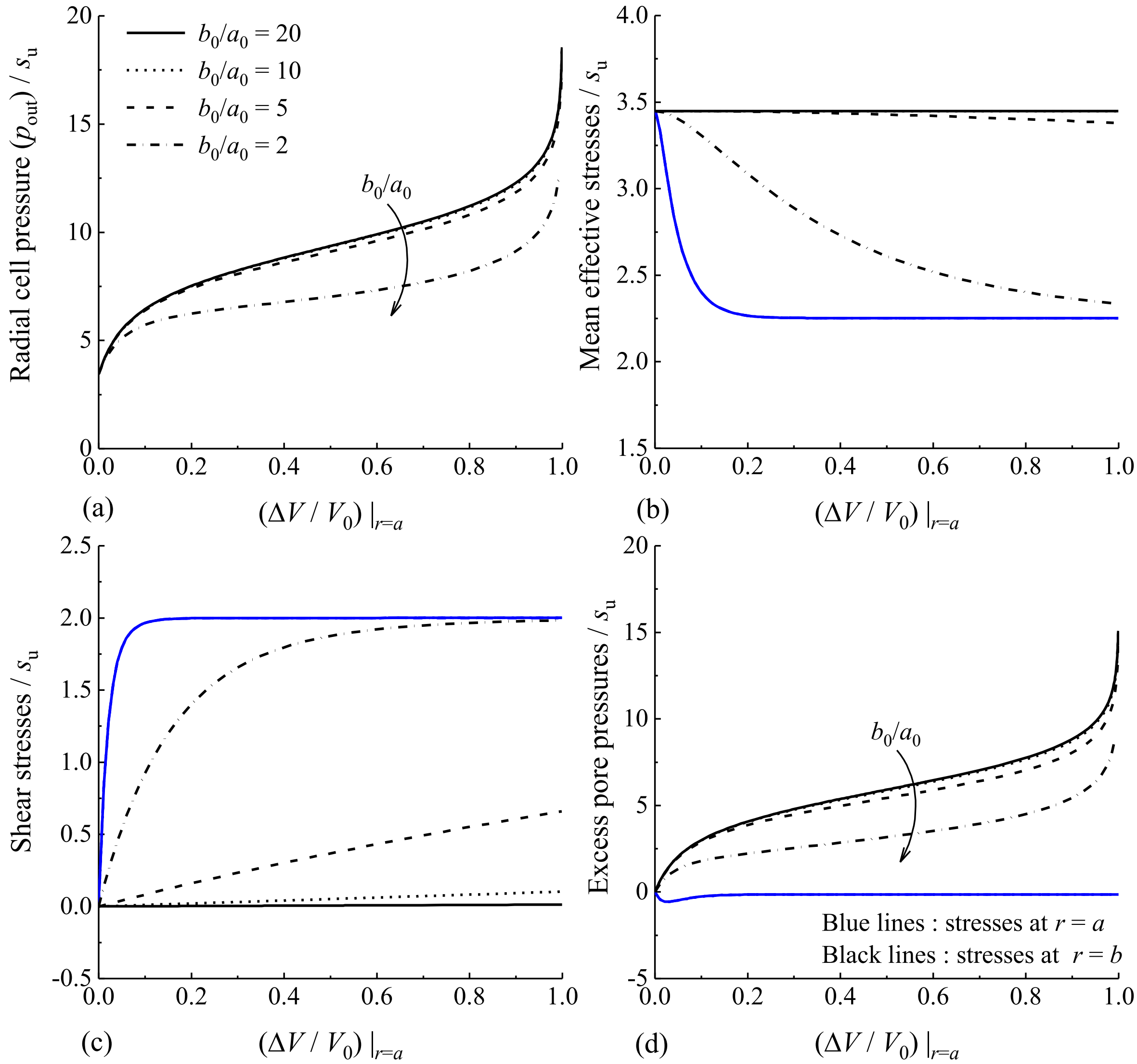

Fig 8. A spherical shell of normally consolidated London clay (R_0=1.001) under external loading.

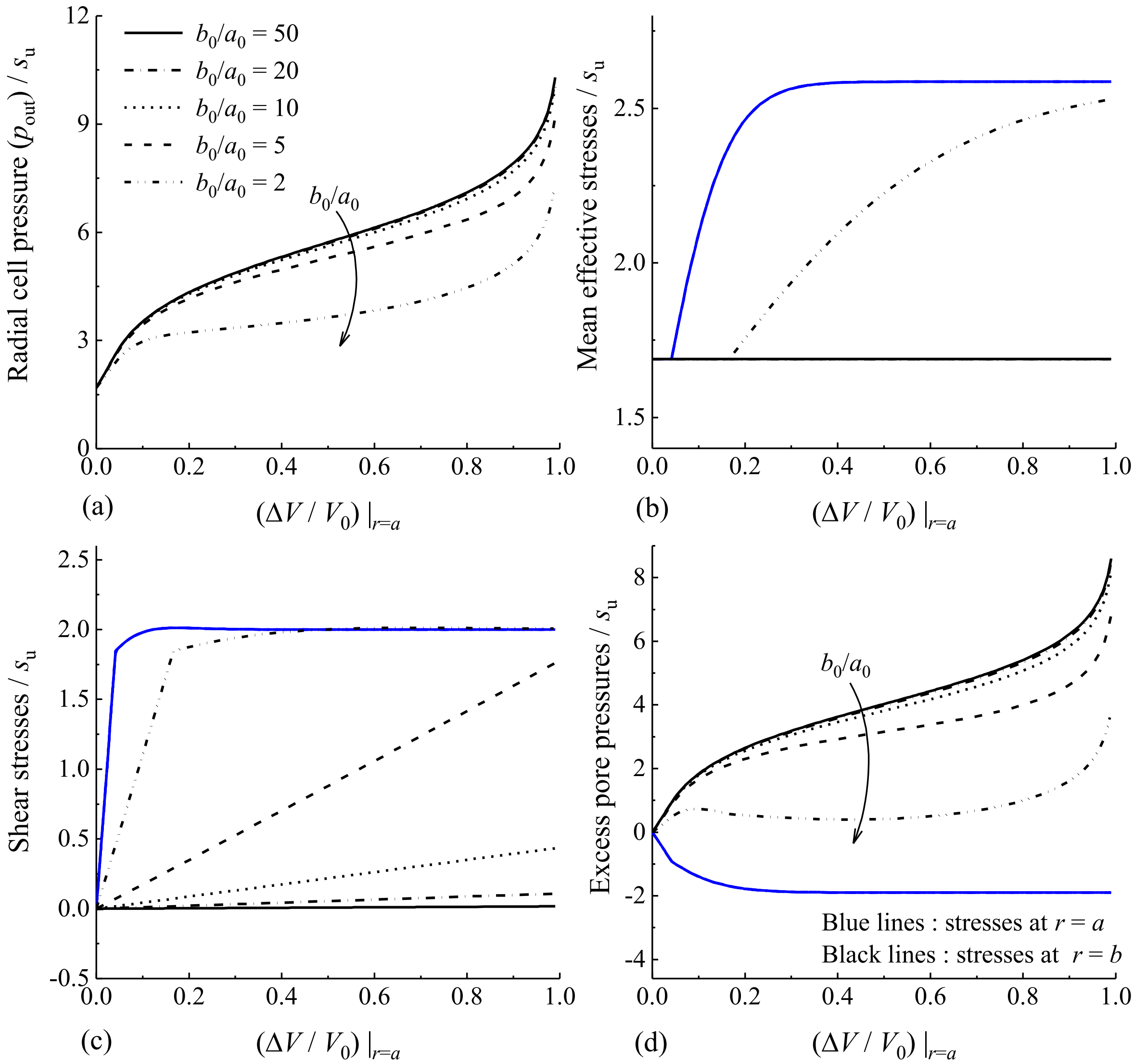

Fig 9. A thick-walled cylinder cavity of stiff London clay (R_0=4) under external loading.

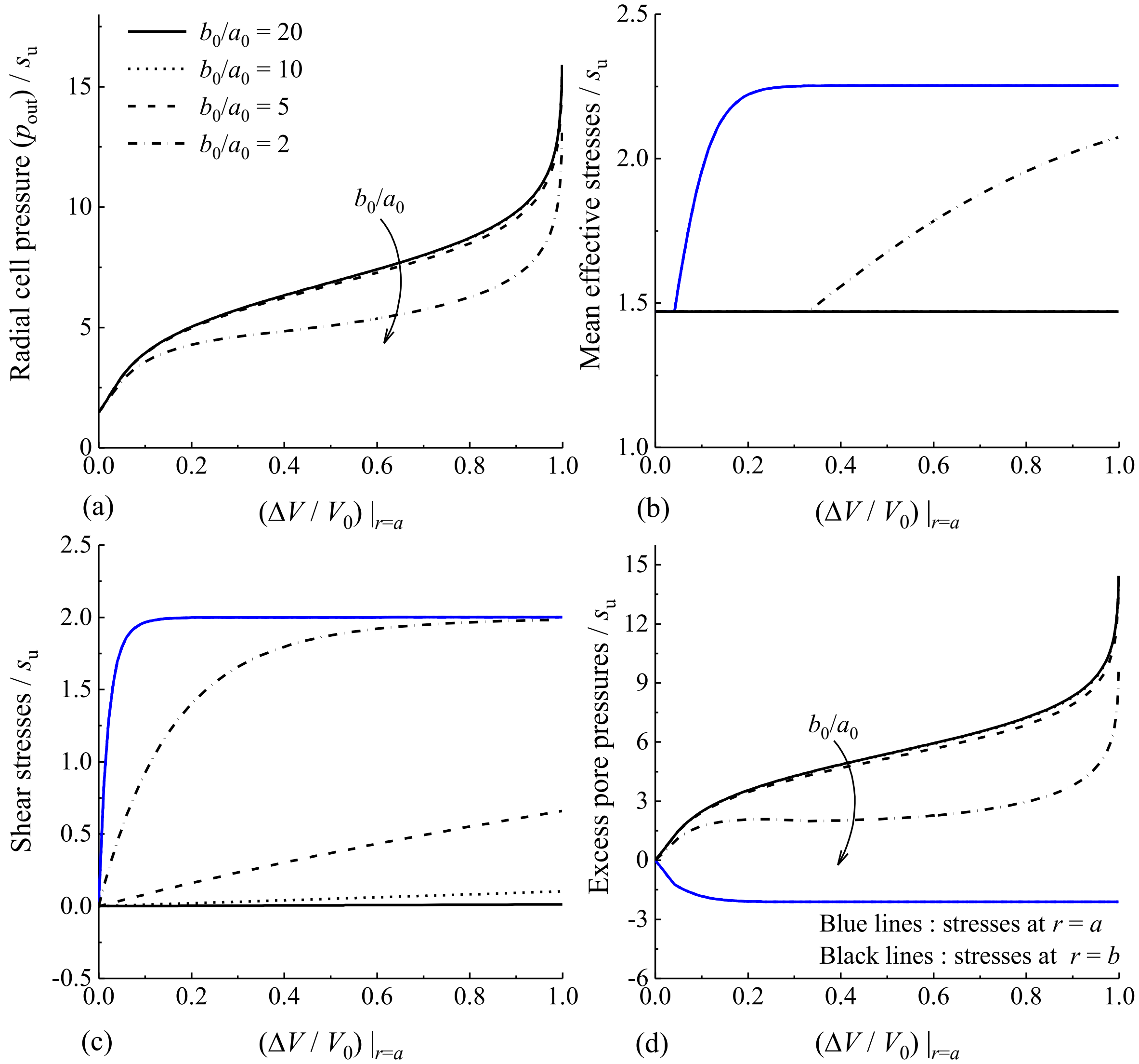

Fig 10. A spherical shell of stiff London clay (R_0=4) under external loading.

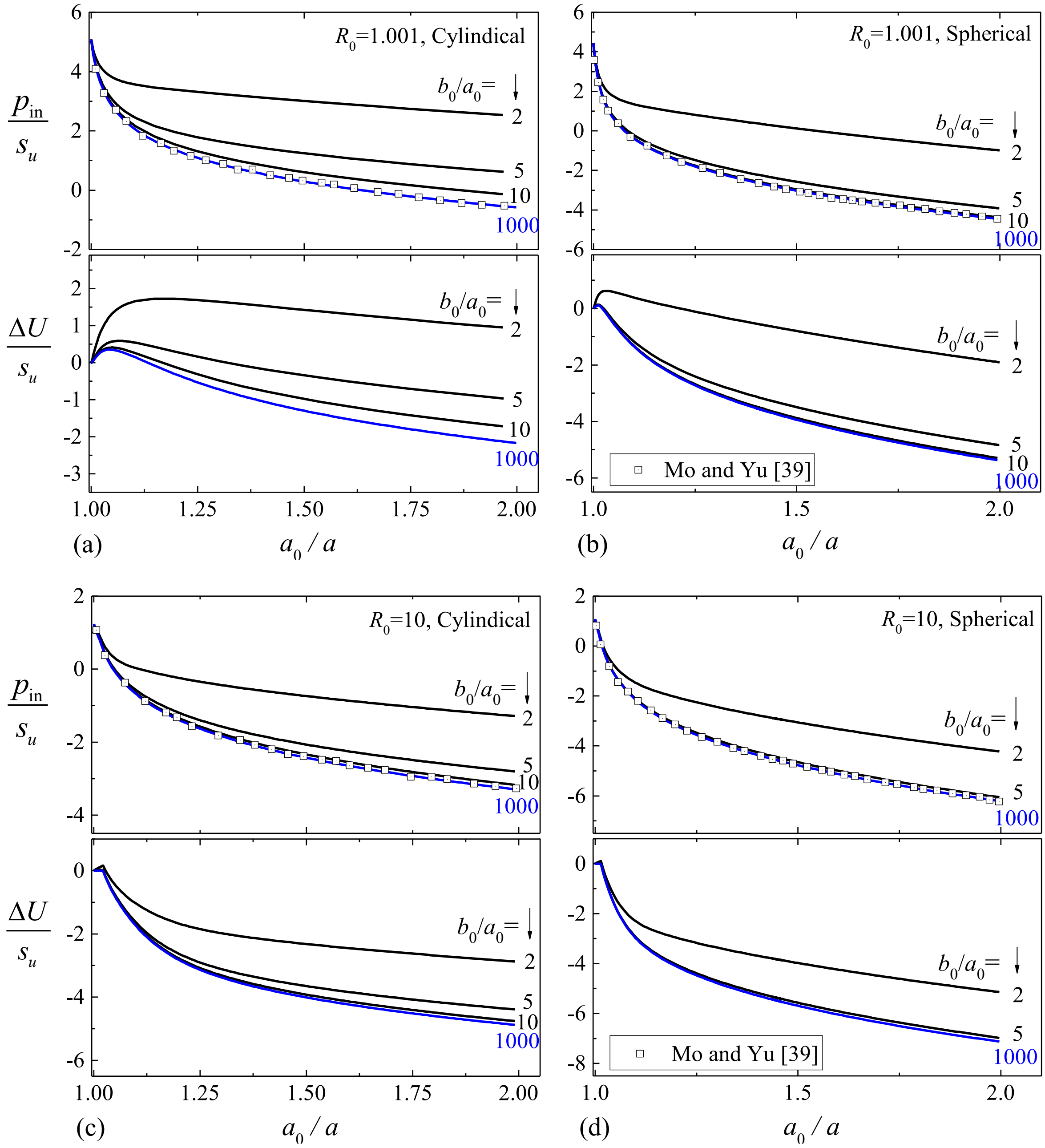

Fig 11. Cavity contraction curves under internal unloading: (a) and (c) cylindrical model; (b) and (d) spherical model.

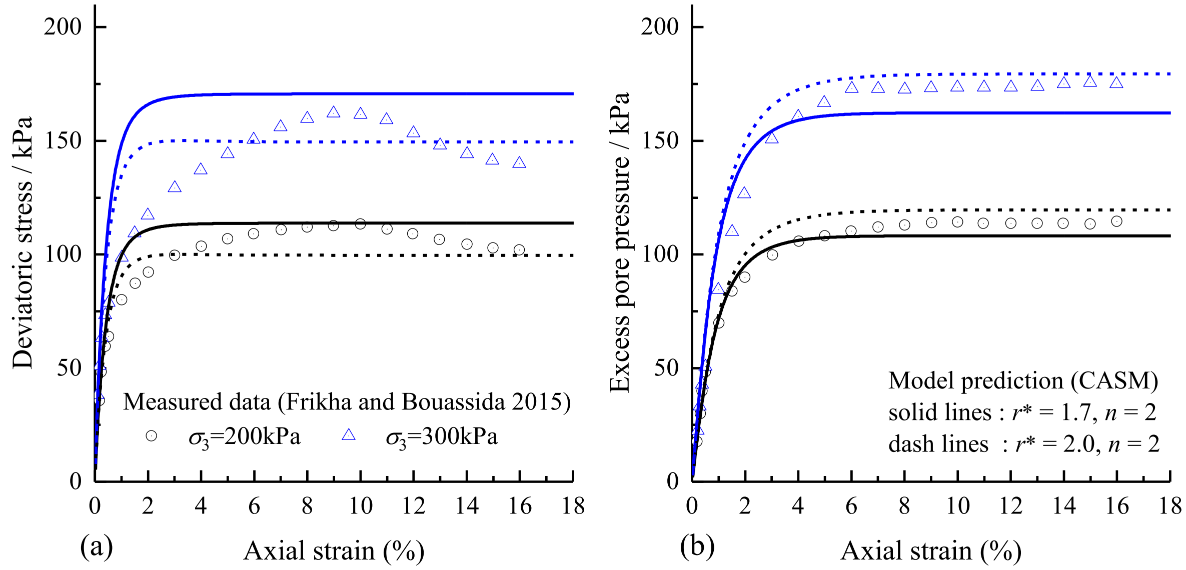

Fig 12. Model prediction for undrained triaxial compression tests with soft Speswhite kaolin.

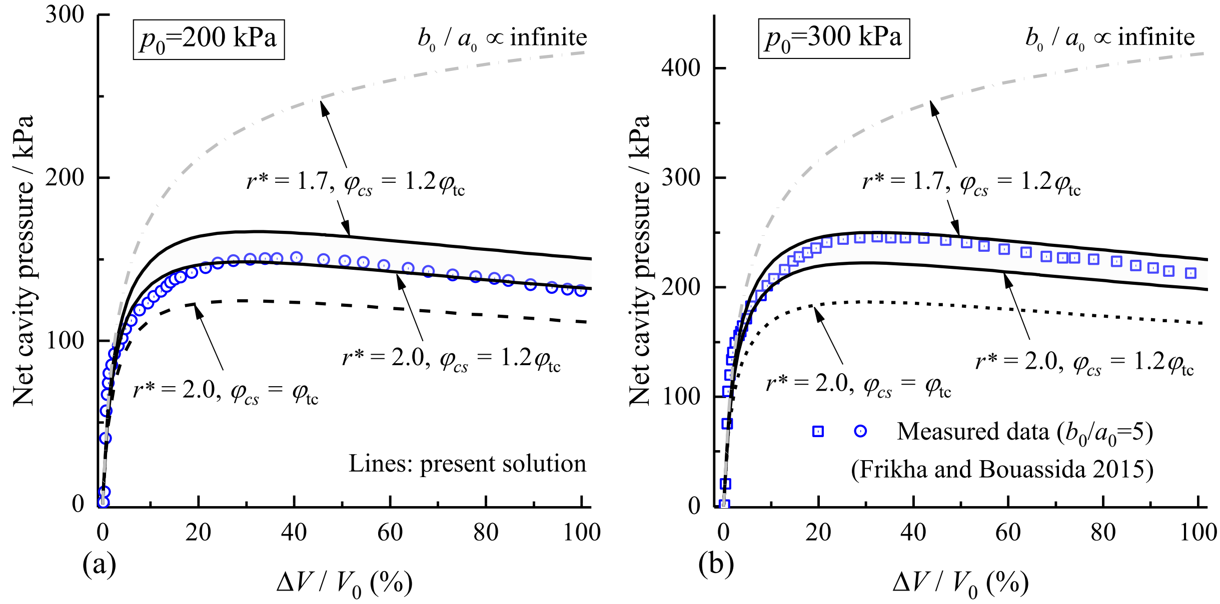

Fig 13. Predicted and measured cavity expansion curves in a thick-walled cylinder of kaolin clay.

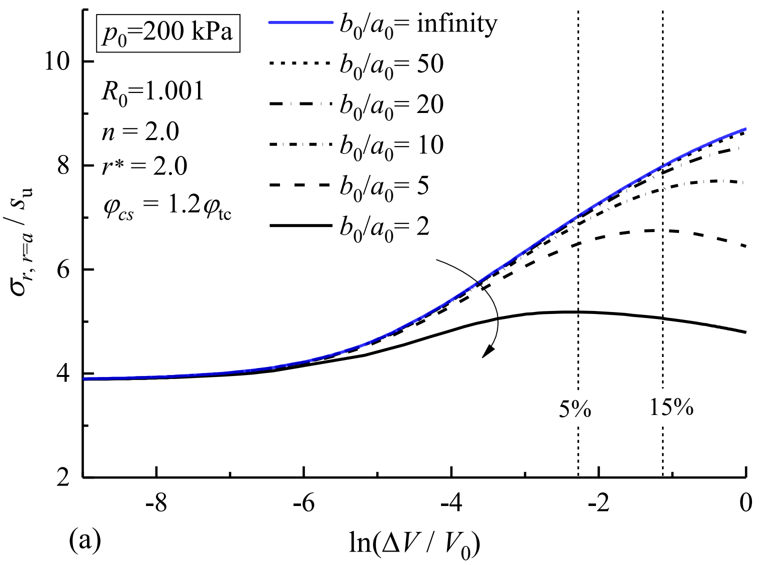

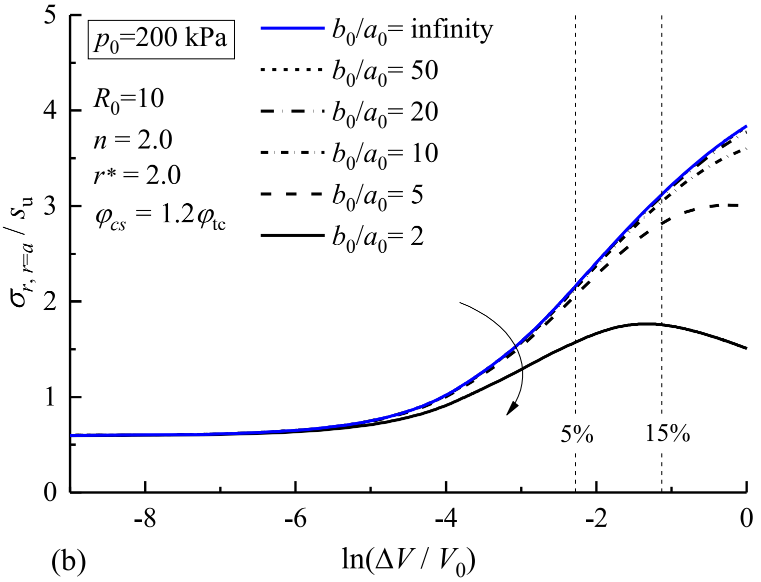

Fig 14. Pressuremeter curves with different values of b_0/a_0 (Speswhite kaolin): (a) normally consolidated clay (R_0=1.001); (b) heavily overconsolidated clay (R_0=10).

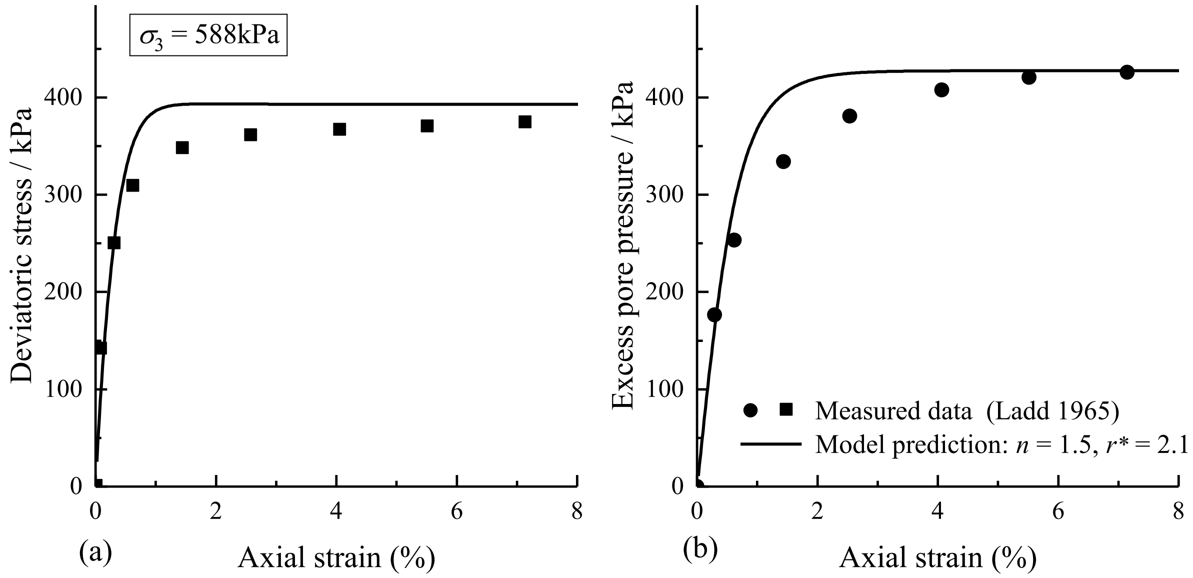

Fig 15. Model prediction for an undrained triaxial compression test on isotropically consolidated RBBC.

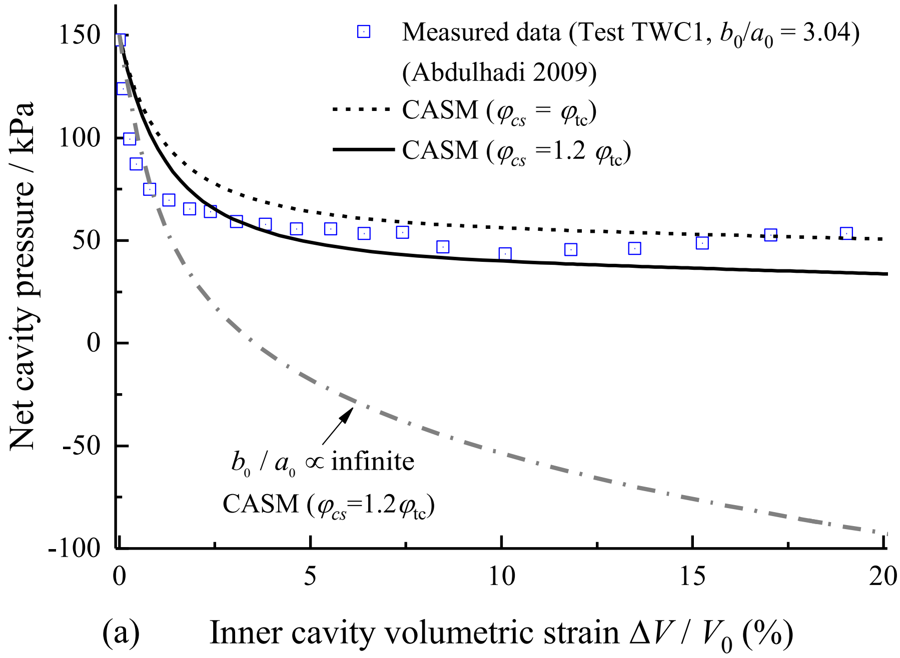

(a)

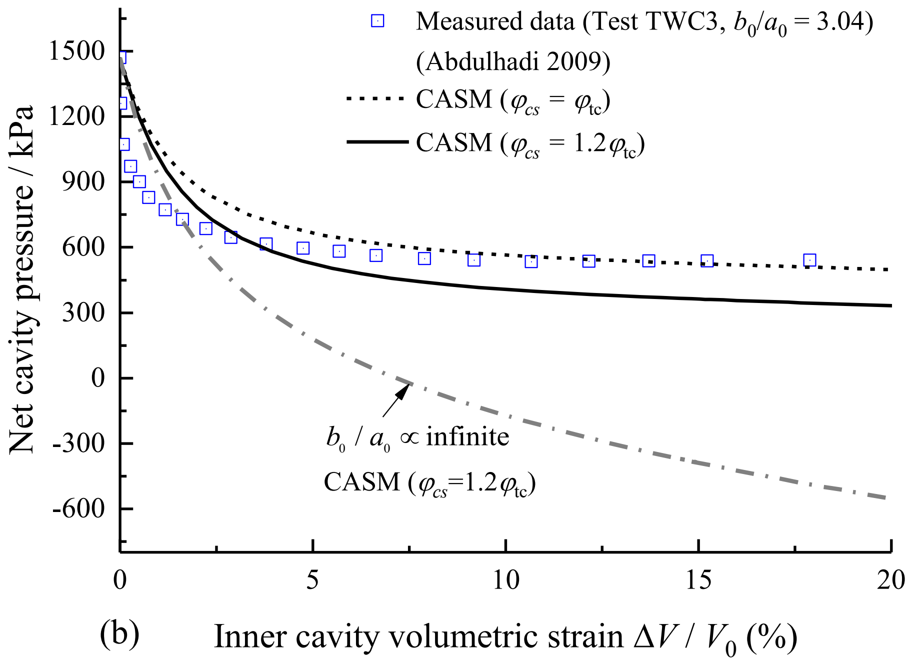

(b)

Fig 16. Predicted and measured cavity contraction curves in thick-walled cylinders of RBBC under internal unloading.

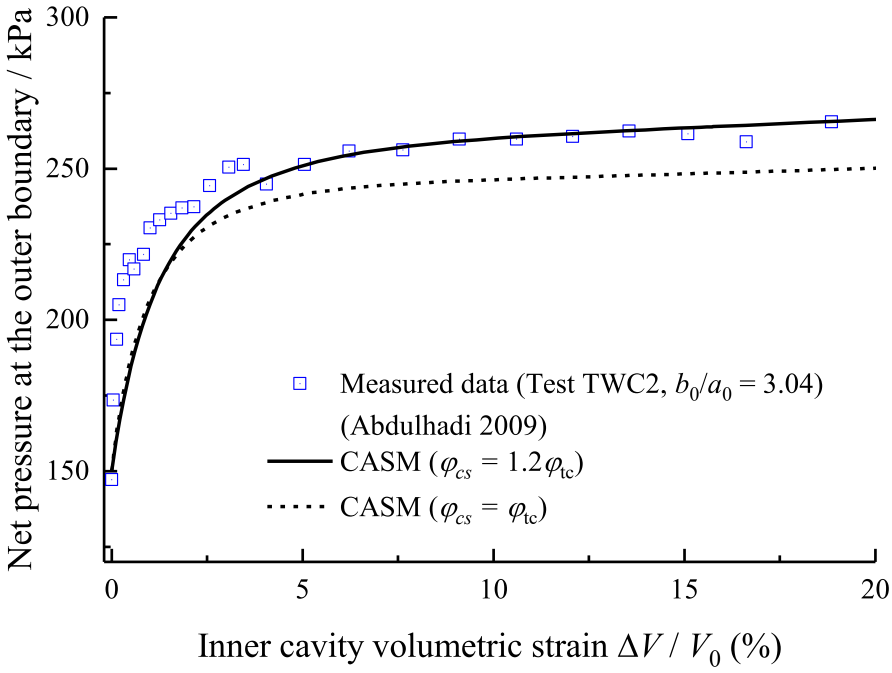

Fig 17. Predicted and measured cavity contraction curves in a thick-walled cylinder of RBBC under external loading.